



저작자표시-비영리-변경금지 2.0 대한민국

이용자는 아래의 조건을 따르는 경우에 한하여 자유롭게

- 이 저작물을 복제, 배포, 전송, 전시, 공연 및 방송할 수 있습니다.

다음과 같은 조건을 따라야 합니다:



저작자표시. 귀하는 원저작자를 표시하여야 합니다.



비영리. 귀하는 이 저작물을 영리 목적으로 이용할 수 없습니다.



변경금지. 귀하는 이 저작물을 개작, 변형 또는 가공할 수 없습니다.

- 귀하는, 이 저작물의 재이용이나 배포의 경우, 이 저작물에 적용된 이용허락조건을 명확하게 나타내어야 합니다.
- 저작권자로부터 별도의 허가를 받으면 이러한 조건들은 적용되지 않습니다.

저작권법에 따른 이용자의 권리는 위의 내용에 의하여 영향을 받지 않습니다.

이것은 [이용허락규약\(Legal Code\)](#)을 이해하기 쉽게 요약한 것입니다.

[Disclaimer](#)

Master's Thesis

Verification and Validation of Monte Carlo Code  
MCS for the Multi-physics High-fidelity Analysis  
of OPR-1000 Multi-cycle Operation

Vutheam Dos

Department of Nuclear Engineering

Graduate School of UNIST

2020

# Verification and Validation of Monte Carlo Code MCS for the Multi-physics High-fidelity Analysis of OPR-1000 Multi-cycle Operation

Vutheam Dos

Department of Nuclear Engineering

Graduate School of UNIST

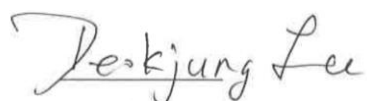
Verification and Validation of Monte Carlo Code  
MCS for the Multi-physics High-fidelity Analysis of  
OPR-1000 Multi-cycle Operation

A thesis  
submitted to the Graduate School of UNIST  
in partial fulfillment of the  
requirements for the degree of  
Master of Science

Vutheam Dos

06. 16. 2020

Approved by



Advisor

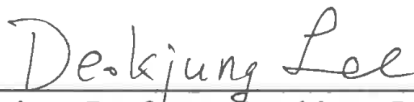
Deokjung Lee


Verification and Validation of Monte Carlo Code  
MCS for the Multi-physics High-fidelity Analysis  
of OPR-1000 Multi-cycle Operation

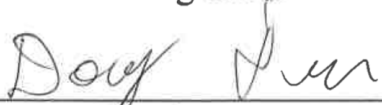
Vutheam Dos

This certifies that the thesis of Vutheam Dos is approved.

06. 16. 2020

  
\_\_\_\_\_  
Advisor: Professor Deokjung Lee

  
\_\_\_\_\_  
Professor Eisung Yoon: Thesis Committee Member #1

  
\_\_\_\_\_  
Professor Douglas A. Fynan: Thesis Committee Member #2

## Abstract

Worldwide demand for high-fidelity simulation tools for large scale power reactor analysis resulted in the coupling of neutronics, thermal hydraulics, and fuel mechanics in nuclear reactor cores. The Computational Reactor Physics and Experiment (CORE) laboratory at Ulsan National Institute of Science and Technology (UNIST) has developed an inhouse Monte Carlo code MCS coupled with multi-physics (MP) tools such as a one-dimensional (1D) single-phase closed-channel thermal-hydraulic code (TH1D), a sub-channel two-phase thermal-hydraulic code (CTF) and a fuel performance code (FRAPCON) to provide thermal-hydraulic and fuel behavior feedbacks for realistic applications. This thesis describes the 3D whole-core analysis with pin-wise resolution in which neutron transport, depletion, thermal-hydraulic, and fuel behavior calculations are performed using the coupled MCS/TH1D, MCS/CTF, and MCS/FRAPCON tools. The OPR-1000 PWR core operated for 2 consecutive cycles is selected as a target for MP coupling analysis, including verification and validation. The OPR-1000 PWR is a Generation II nuclear reactor in South Korea with 2815 MW thermal power modeled explicitly in MCS. The MCS simulation of OPR core during the zero-power physics testing was evaluated for critical boron concentration (CBC) and control rod worth, and the results show good agreement with the references. The verification and validation of MCS MP coupling were conducted at hot full power conditions along with various feedback required for reactor power simulation such as depletion, equilibrium xenon update, CBC search, and on-the-fly cross-section reconstruction. The influence on other parameters, including CBC, axial shape index, pin- and assembly-wise radial/axial power profiles, fuel temperatures, and moderator temperatures/densities, were investigated. The MCS MP coupled results were also compared against the experimental data for validation. Additional comparisons were made with the data from the plant's nuclear design report and result from the deterministic two-step code STREAM/RASTK 2.0 (ST/R2) and 3D Method of Characteristic (MOC) direct neutron transport code STREAM. For the MCS MP coupling tool with thermal-hydraulic and fuel performance feedback, excellent agreement is observed with the measured values with a root mean square (RMS) error of 26 ppm for CBC and 1.8% for assembly power. Compared to other codes, MCS MP coupling results have an RMS error of 16 ppm for CBC and 1.8% for assembly power. Larger discrepancies in relative assembly power between MCS based MP tool and measured data occur in the core-periphery where the power is relatively low, while at the end of cycles, the discrepancies are still within 1 standard deviation of about 2.4%. This study demonstrates MCS's capability to perform high-fidelity simulation of a practical light water reactor core.

*This page is intentionally left blank*

## Table of Contents

I. Introduction	1
1.1. Objective of the thesis	2
II. Analysis Methodology	2
2.1. MCS Monte Carlo code	2
2.2. MCS coupling mechanism	4
2.2.1. MCS/TH1D coupling	5
2.2.2. MCS/CTF coupling	7
2.2.3. MCS/FRAPCON Coupling	11
III. Verification and Validation of MCS Multi-physics Coupling Model	14
3.1. Fuel pin model	14
3.2. 16x16 assembly and 2x2 core model	15
3.3. OPR-1000 core	16
3.4. Code for comparison	17
3.4.1. STREAM/RASTK2 (ST/R2)	17
3.4.2. STREAM-3D (ST3D)	17
3.4.3. Nuclear Design code	17
IV. Verification and validation of the MCS MP coupling system	17
4.1. Fuel pin	17
4.2. 16x16 assembly	20
4.3. Checkboard 2x2 assemblies	23
4.4. Multi-physics full core results	25
4.4.1. The Zero Power Physics Testing verification	25
4.4.2. MCS/TH1D cycle01	26
4.4.3. MCS multi-physics couplings vs. Measured data	33
4.5. MCS Multi-cycle Simulation Analysis	44
V. Conclusion and Perspective	49
REFERENCES	50



## List of Tables

Table 1. The comparison of computation code for MCS couplings.....	14
Table 2. Pin model in MCS and parameters.....	15
Table 3. Summary of calculated pin results. ....	19
Table 4. Summary of the calculated results of the fuel assembly test.....	21
Table 5. Summary of MCS calculated results for 2x2 core. ....	24
Table 6. Summary of MCS V&V error statistics for OPR-1000.....	28
Table 7. Summary of relative error in radial assembly power distribution.....	28
Table 8. Summary of the simulation time and memory in MCS.....	34
Table 9. Summary of calculated fuel and outlet temperature in MCS couplings.....	34
Table 10. Summary of CBC results and the CBC difference against measured data.....	34
Table 11. Summary of relative radial power differences of MCS compared to measured data. ....	35
Table 12. Summary of MCS/TH1D V&V of the relative power differences <sup>a</sup> .....	45

## List of Figures

Figure 1. Flow chart of MCS feedback and multi-physics couplings.....	5
Figure 2. Diagram of single-channel TH1D analysis axial direction (left) and the heat conductance analysis in a radial direction (right). .....	6
Figure 3. Flow chart of MCS/TH1D coupling interface with Picard iteration methods. ....	7
Figure 4. Neutronics and CTF subchannel model in MCS. ....	10
Figure 5. Flow chart of MCS/CTF coupling interface with Picard iteration methods.....	10
Figure 6. Flow chart of the MCS/FRAPCON coupling interface. ....	13
Figure 7. 16x16 OPR fuel assembly (left) and 2x2 checkboard core (right). ....	16
Figure 8. Loading patterns of Cycle 1 (left) and Cycle 2 (right). ....	16
Figure 9. Comparison of pin test results of axial power, fuel temp, coolant temperature and density of MCS multi-physics couplings.....	19
Figure 10. Comparison of pin test results of axial power, fuel temp, coolant temp. and density of MCS multi-physics couplings with constant gap-conductance in FRAPCON. ....	20
Figure 11. Axially integrated results of a fuel assembly in MCS coupling.....	22
Figure 12. Pin-wise distribution in fuel assembly problem of MCS coupled systems. ....	22
Figure 13. MCS/CTF and MCS/FARAPCON pin-wise distribution differences compared to MCS/TH1D.....	23
Figure 14. Axially integrated results of 2x2 core in MCS couplings.....	24
Figure 15. Pin-wise distribution of checkboard 2x2 core in MCS coupled systems. ....	25
Figure 16. MCS/CTF and MCS/FARAPCON pin-wise differences compared to MCS/TH1D. ....	25
Figure 17. Verification of ZPPT at the beginning of reactor life (BOC, HZP, no Xe).....	26
Figure 18. MCS/TH1D V&V of boron letdown curve and ASI results. ....	28
Figure 19. MCS radial assembly power distribution and relative error at BOC Cycle 01.....	29
Figure 20. Axial power distribution at BOC Cycle 01.....	29
Figure 21. MCS radial power distribution and axial power distribution comparison at MOC (6.0 MWD/MT) Cycle 01; NDR = 5 MWD/MT.....	30
Figure 22. Relative error of radial assembly power distribution at MOC Cycle 01. ....	30
Figure 23. MCS radial power distribution and axial power distribution comparison at EOC (13.8 GWD/MT) Cycle 01. ....	31
Figure 24. Relative error of radial assembly power distribution at EOC Cycle 01. ....	31
Figure 25. Axially integrated pin-power and uncertainty of MCS/TH1D at BOC and EOC.....	32
Figure 26. Axially integrated pin-by-pin distribution of MCS/TH1D at BOC and EOC. ....	32
Figure 27. Axial distribution of MCS/TH1D against ST/R2 at BOC (left) and EOC (right). ....	33

Figure 28. Boron letdown curves and ASI of MCS MP coupling against measured data. ....	36
Figure 29. NDR assembly power (top left) and relative error compared to MCS MP coupling results at BOC (0.05 GWD/MT) Cycle 01.....	37
Figure 30. Measured assembly power and relative error compared to MCS MP couplings at MOC (6.0 GWD/MT) Cycle 01. ....	38
Figure 31. Measured assembly power and the relative error of MCS MP couplings at EOC (13.8 GWD/MT) Cycle 01. ....	38
Figure 32. MCS MP couplings results of axial power distribution against the measured data.....	39
Figure 33. Axial distribution of MCS against ST/R2 at BOC (left) and EOC (right) Cycle 01. ....	39
Figure 34. MCS axial fuel temperature, thermal conductivity, and gap conductance comparison at BOC (0.0 Gwd/MT). ....	39
Figure 35. MCS axial fuel temperature, thermal conductivity, and gap conductance comparison at EOC (13.8 GWD/MT). ....	40
Figure 36. Power distribution of MCS and relative differences at BOC Cycle 01. ....	41
Figure 37. Power distribution of MCS and relative differences at EOC Cycle 01. ....	41
Figure 38. Fuel temperature distribution of MCS and relative differences at BOC Cycle 01. ....	42
Figure 39. Fuel temperature distribution of MCS and relative differences at EOC Cycle 01. ....	42
Figure 40. Coolant temperature distribution of MCS and relative differences at BOC Cycle 01.....	43
Figure 41. Coolant temperature distribution of MCS and relative differences at EOC Cycle 01.....	43
Figure 42. Coolant density distribution of MCS and relative differences at BOC Cycle 01. ....	44
Figure 43. Coolant density distribution of MCS and relative differences at EOC Cycle 01. ....	44
Figure 44. U-235 density at Cycle 01 EOC (left) and Cycle 02 BOC (right).....	45
Figure 45. MCS/TH1D V&V of boron letdown and ASI results in Cycle 02. ....	46
Figure 46. MCS/TH1D radial assembly power and relative error at Cycle 02 BOC.....	47
Figure 47. MCS radial assembly power and relative error at Cycle 02 MOC. ....	47
Figure 48. MCS radial assembly power and relative error at Cycle 02 EOC. ....	48
Figure 49. MCS/TH1 axial power distribution Cycle 02.....	48
Figure 50. Pin-wise distribution at BOC and EOC Cycle 02.....	49

## I. Introduction

The nuclear reactor design should satisfy all safety criteria, and the computational codes must be reliable and efficient to predict expected and unexpected events during operation. Several factors, such as heat transfer, fluid flow, and structural mechanics, significantly influences fuel pin temperature, coolant temperature, and density, which must be considered for nuclear operation stabilization and safety. Several concerns have been raised regarding the impact of increased core fuel temperature on power distribution [1], and exposure of fuel and cladding materials to high temperature, high pressure, and neutron flux due to the irradiated fuel rod in the core, on fuel behavior [2]. The understanding and prediction of these behaviors are essential for safe and economical operation and can be achieved by the reactor thermal-hydraulic (TH) and fuel performance (FP) codes. The neutronics and the TH parameters have strong effects on thermal feedback in both steady and transient states of the reactor core but are traditionally performed separately. The neutronics calculation is usually performed with constant thermal properties of the fuel or coolant during the simulation. In contrast, FP calculations use approximate values, or the required parameters, such as power distribution, fission production, and flux, are calculated externally [2]. The strong feedback between fission power, fuel temperature, and coolant density cannot be separated because each partial solution builds up the next calculation source. The use of constant approximations or performing the individual calculations will yield reliable solutions and limit the wide use of the code due to problem dependence.

Coupling the neutronics to TH or/and FP for the entire core under steady and transient states, often categorized as “multi-physics (MP),” has become a desired feature in advanced high-fidelity analysis tools. The high-fidelity MP tools usually employ the deterministic rather than the Monte Carlo (MC) methods for economic and fast simulation. However, there are concerns about its efficiency and accuracy due to the use of approximations. In contrast, the MC methods use continuous neutron cross-sections, with flexible or complicated geometry, and do not require approximations. The MC method can provide the most accurate solution for the 3D particle transport problem and is well suited for nuclear reactor investigations. Despite these advantages, the MC code downsides include increased prohibitive computational time for acceptable statistics, high memory required for cross-sections and tallies, and accounting for MP feedback. However, the availability of relatively cheap, large-scale computing, along with the recent advancements in computer capacity and continued demand for high-performance MP tools, have triggered the fast development of high-fidelity reactor MP simulation tools by many groups worldwide.

In the last few decades, various MC codes such as MC21 [3], Research Monte Carlo (RMC) [4], OpenMC [5], and Serpent2 [6] have been rapidly developed along with various methods, techniques and advanced features to account for high-fidelity simulation. For instance, the continuous-energy RMC codes are coupled with Coolant Boiling in Rod Arrays-Two Fluids (COBRA-TF; hereafter, CTF) sub-

channel TH code by adapting the hybrid coupled scheme [7]. MC21 was also coupled with CTF using a consortium for advanced simulation of the light water reactor (LWR) (CASL) tool [3,8]. The development of the MP interfaces [9] by Serpent2 improved its capability to couple with TH SubChanFlow [10] and FP ENIGMA [11]. For developing high-fidelity simulation tools for large scale nuclear power analysis, the Computational Reactor Physics and Experiment (CORE) group at Ulsan National Institute of Science and Technology (UNIST) is developing an in-house MC neutron transport code from scratch since 2014, named as MCS [12] and was recently coupled to TH code (TH1D, CTF) and FP code (FRAPCON). It was successfully applied for the BEAVRS core benchmark for 2 cycles [13-18] and VERA whole core [19].

### **1.1. Objective of the thesis**

The specific goal of this study is to develop and demonstrate the MCS MP coupling capability with different feedback such as TH coupling (MCS/TH1D and MCS/CTF) and FP coupling (MCS/FRAPCON) for realistic core applications. This work provides details of each feedback's unique characteristics and addresses the advantages of MP coupling schemes and illustrates the accuracy and efficiency of each coupled code for the OPR-1000 core system. The initial neutronics/TH coupling of the MCS codes will be demonstrated using the one-dimensional (1D) single-phase closed channel model, MCS/TH1D. The MCS/TH1D feedback is based on a 1D single-phase closed channel model with no cross-flow between the neighboring channels. MCS sends the fuel pin power distribution to the solver, and the calculated coolant density and fuel/coolant temperature distributions based on the inlet temperature and flow rate in TH1D will be updated to MCS. The MCS/CTF is similar to TH1D as it receives power from MCS and updates the coolant density and fuel/coolant temperature distributions. However, CTF is a three-dimensional (3D) sub-channel of TH code that formulates the given sets of conservation equations using a simplified sub-channel approach. The neutronics/FP coupling of MCS code is demonstrated using the FP FRAPCON which is also based on a 1D TH pin-cell solver like TH1D but receives the power distribution and burnup interval from MCS to solve the Bateman equations, and determines the fuel burnup, thermal conductivity, and gap conductance accordingly. Finally, the MCS updates the coolant densities and coolant/fuel temperatures for the next transportation step from the FRAPCON results.

## **II. Analysis Methodology**

### **2.1. MCS Monte Carlo code**

MCS is a 3D continuous-energy neutron/photon particle transport code based on the MC method under development at Ulsan National Institute of Science and Technology (UNIST) since 2014 [12].

The MCS code aims at developing a high-fidelity tool capable of supporting large-scale nuclear reactor analysis such as PWRs. MCS has features required for the PWRs criticality and depletion analysis, and the neutron/photon fixed source runs for shielding analysis. MCS neutron transport capability had been verified and validated against several benchmarks, including 279 cases from the International Criticality Safety Benchmark Experimental Problem (ICSBEP), the BEAVRS benchmark, VENUS-2 and Hoogenboom benchmarks [20]. MCS pin-wise depletion capability with TH and/or FP feedback has also been validated against the solution of BEAVRS [13-18], VERA benchmark [19], PWR data from Westinghouse [21] and OPR-1000 reactor [22]. MCS analysis works have also been applied to different application such as very high-temperature reactors [23], the Jordan Research Training Reactor [24], PWR spent fuel pool and storage cask [25], the long-cycle small modular lead cool fast reactor [26], spent fuel cask shielding [27], and the China Experimental Fast Reactor [28].

MCS has adopted various algorithms and optimizations methods to accelerate the calculation and effective use of memory during the depletion simulation and to store the high-accuracy results. For instance, MCS adopted the hash indexing algorithm that allows effective calculation of the base index and quickly retrieves the tally bin index. In addition, MCS calculates the Shannon entropy and center of mass to check the fission source distribution convergence. Additionally, MCS employed the modified power and coarse mesh finite difference methods to accelerate the fission source convergence for criticality calculation. Parallel computing, such as message passing interface (MPI) and OpenMP, which can optimize the memory requirement per processor and decrease unnecessary communications between processors, are also available in MCS [29].

For the high-performance of power reactor simulation, five feedback kernels are implemented in MCS, namely, the multi-cell depletion, on-the-fly (OTF) neutron cross-section Doppler broadening feedback (OpenW), equilibrium xenon, critical boron concentration (CBC) search, and TH feedback. The MCS depletion capability is implemented by adopting the Chebyshev Rational Approximation Method (CRAM) to solve the Batman equation and uses the Gauss-Seidel iterative method to accelerate the depletion calculation in the CRAM solver. The semi and full predictor-corrector schemes are also implemented in MCS to help simulate continuous changes in the reaction rates at each burnup step. In addition to the depletion capability, the equilibrium xenon feedback implemented in MCS helps prevent the unphysical oscillation induced by the statistical uncertainty of xenon number density. MCS features a verity of temperature-dependent neutron data and supports probability tables at different energy ranges. MCS uses the windowed multipole representation technique to calculate the OTF doppler broadening cross-section at the resolved resonance range. MCS uses the interpolation technique based on the probability data to treat the unresolved resonance energy range. The TH feedback implemented in MCS based on the MP coupling with the TH code (TH1D, CTF) and/or FP code (FRAPCON), is described in the next section. The flow chart of the main feedback algorithm implemented in MCS code is shown in Figure 1. At the end of every transport cycle, MCS updates the TH condition, xenon number density,

and boron concentration and performs the convergence check. The flexibility and applicability of MCS make it an eligible tool in large-scale power reactor cores.

## **2.2. MCS coupling mechanism**

The MP coupling, referred to as the neutronics code coupling with the TH and/or FP code, combines each of the code's strengths to improve the accuracy and prediction capabilities of the coolant and fuel feedback effects on power reactor core. The neutronics is particularly focused on subsequent fission energy deposition calculations which influence the reactivity, flux, power or cross-section generation; the TH solver investigates the effect of heat transfer and fluid mechanics due to the changes in coolant properties, while FP investigates the mechanical behavior of the fuel and cladding material in the fuel rod. Therefore, data transfer between the neutronics to/from the TH and/or FP module must be acquired for high-accuracy simulation tools. MCS has developed the MP coupling interface by adopting the cycle-wise Picard iteration method to exchange its data with the coupling solver. The MCS structure is suitable for MP coupling as MCS can produce data as input for other modules (TH, and FP), and can also save the output from other modules. The coupling of these codes with MCS creates a single-executable MP coupled-code application. Figure 1 shows the algorithm of the MCS coupling interface with other solvers. At each MCS neutron transport simulation, the calculated instant power distribution results will be sent as the input parameter for the stand-alone coupling solver (TH or/and FP). After simulation, the stand-alone solver updates the fuel temperature, coolant temperature and density at the end of each iteration. In general, the important parameters to solve the neutron flux at the current neutron transport cycle are the nuclide density and temperature distribution of the previous cycle. Therefore, MCS will use these updated material and coolant feedback properties along with the temperature for the next MC neutron transport calculation. The repeated process of data transfer between neutronic and coupled solver will be done until the convergence criteria for MCS neutron transport are met.



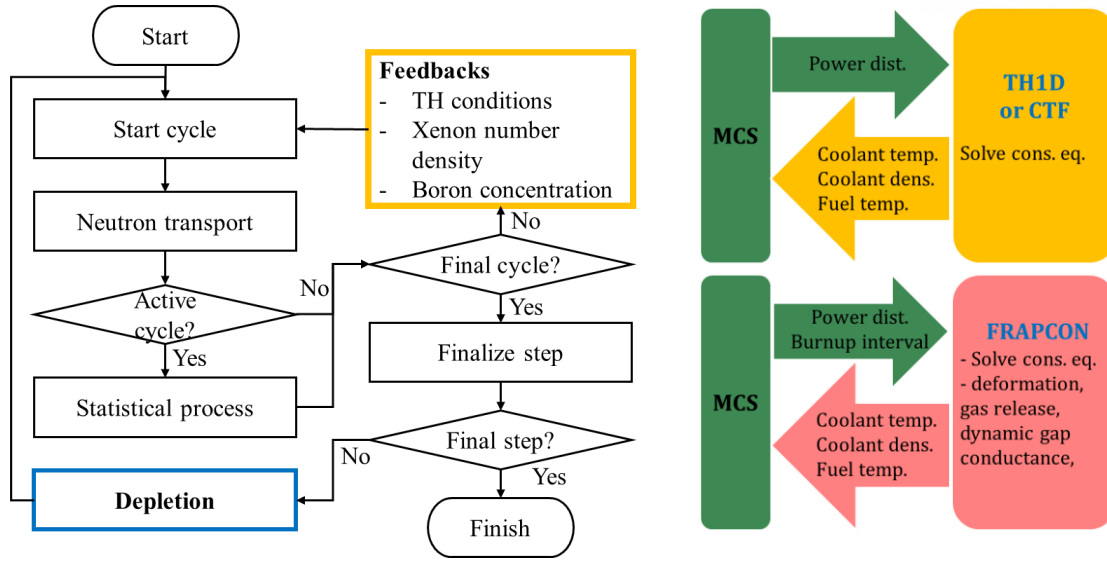


**Figure 1. Flow chart of MCS feedback and multi-physics couplings.**

### 2.2.1. MCS/TH1D coupling

TH1D is a closed channel solver that can solve TH equation based on pin-by-pin geometry, and was originally developed by the Seoul National University to be used with nTRACER direct whole core calculation code [30]. TH1D solver accounts for the equal mass flow rate of each pin axially under the condition of unheated incompressible flow. There is no net mass (cross-flow) exchange between the neighboring channels. Even though the TH1D has fast computing time and simple user input, it is not realistic because it does not account for the two-phase model. The moderator temperature and void fraction are implicitly included in the moderator density feedback by considering constant pressure. In a single flow, the TH1D solves 1D equations in an axial direction of the mass and energy conservation at a steady-state to get the coolant temperature/density at each single coolant channel, as expressed in Eq. (1); the diagram illustrating the TH analysis is in Figure 2 (left).

$$\begin{aligned}
 \text{Mass conservation equation} &: \frac{\partial \rho}{\partial t} + \frac{\partial \rho v}{\partial z} = 0 \\
 \text{Energy conservation equation} &: \frac{\partial \rho h}{\partial t} + \frac{\partial \rho h v}{\partial z} = q_c + \frac{\xi}{A_c} q_w \equiv q
 \end{aligned} \tag{1}$$

$$\text{where} \begin{cases} \rho = \text{Coolant density (Kg/m}^3\text{)}; & h = \text{Coolant enthalpy (J/Kg)} \\ v = \text{Speed of coolant (m/s)}; & \xi = \text{Coolant heated perimeter (m)} \\ A_c = \text{Cross-section channel (m}^2\text{)}; & q_c = \text{Coolant heat source (W/m}^3\text{)} \\ q_w = \text{fuel heat flux (W/m}^2\text{)} \end{cases}$$

The axial heat conduction is neglected, and the fuel rod is divided into many rings to get the radial temperature distribution; there are 10 rings in the MCS default option, as illustrated in Figure 2 (right). The heat conduction formula in the radial direction is expressed as:



$$C_p \frac{\partial T}{\partial t} = \frac{1}{r} \frac{\partial}{\partial r} \left( k(T) r \frac{\partial T}{\partial r} \right) + q \quad (2)$$

where  $\begin{cases} C_p = \text{production of heat capacity (J/cm}^3 \cdot \text{ }^\circ\text{C)} \\ k(T) = \text{heat conductive model (W/cm} \cdot \text{ }^\circ\text{C)} \\ v = \text{volume heat source (W/cm}^3\text{)} \end{cases}$

In TH1D solver, the default thermal conductance of the gap between fuel pellets and cladding is set to 10,000 W/m-K and thermal conductivity of the fuel pellets and cladding based on MATPRO-9 is expressed as:

$$\begin{aligned} K_{UO_2,0.95} &= 1.05 + 2150(T - 73.15)^{-1} \text{ (W/m} \cdot \text{K)} \\ K_{clad} &= 7.51 + 2.09 \times 10^{-2} T - 1.45 \times 10^{-5} T^2 + 7.67 \times 10^{-9} T^3 \text{ (W/m} \cdot \text{K)} \end{aligned} \quad (3)$$

where T is the temperature (K),  $k_{clad}$  is the cladding thermal conductivity, and  $k_{UO_2,0.95}$  is the thermal conductivity of fuel pellet with a density fraction of 95% to the theoretical density (theoretical density is taken as 10.96 g/cm<sup>3</sup>). The steam table of IAPWS-IF97 is implemented as a polynomial and used in TH1D within the temperature range of 280 °C to 340 °C at 15.5 MPa.

Figure 3 illustrates the Picard iteration flow chart for exchanging data between MCS and TH1D coupling. First, MCS performs the transport calculation and sends power distribution in a single pin tallied to TH1D solver. TH1D does not require core geometry information or pin location from MCS because it is a closed channel. The TH1D then solves the one-dimensional thermal/hydraulic equation with the given power distribution from the MCS transport calculation. The convergence of fuel temperature will be checked in each iteration by comparing the temperature of current iteration  $i$  with the temperature of previous iteration  $i-1$ . If it is not yet converged, the fuel and coolant conditions will be updated and then repeated from the transportation calculation step until it is converged.

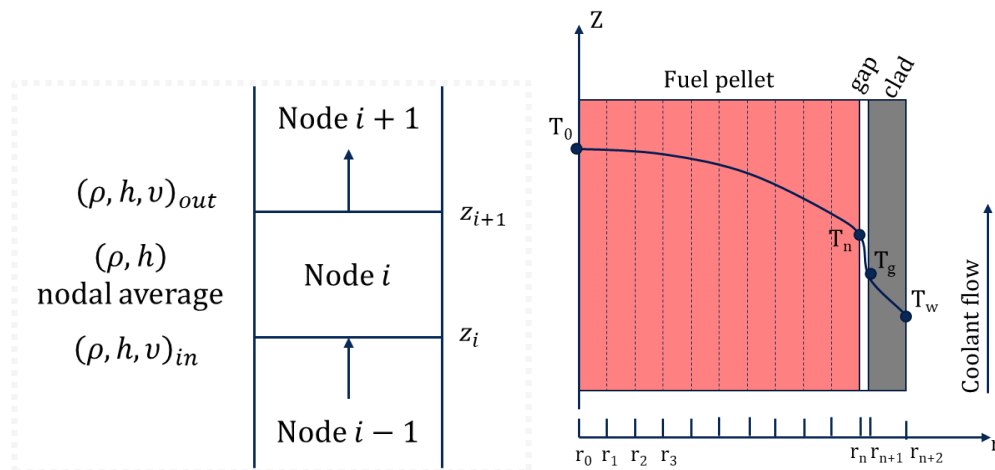


**Figure 2. Diagram of single-channel TH1D analysis axial direction (left) and the heat conductance analysis in a radial direction (right).**

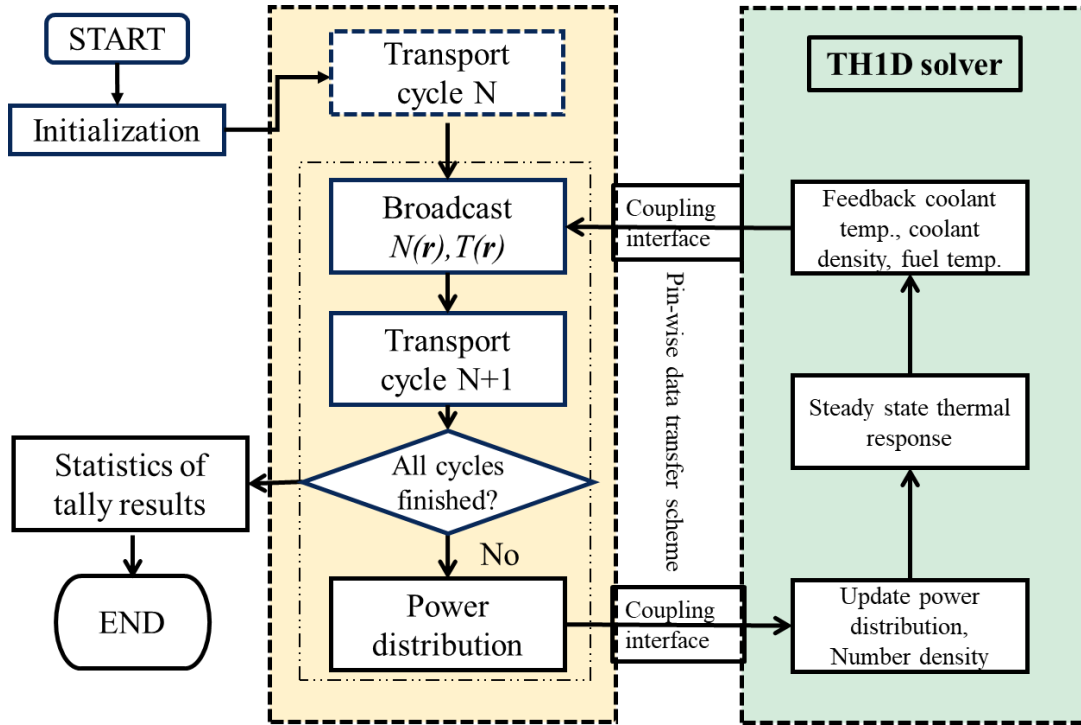


**Figure 3. Flow chart of MCS/TH1D coupling interface with Picard iteration methods.**

### 2.2.2. MCS/CTF coupling

CTF is a sub-channel TH simulation code designated for assessing LWR behavior [31]. CTF was first developed by the Pacific Northwest Laboratory and the Pennsylvania State University. It was then adopted into the Consortium for advanced simulation of LWR in 2012 and then served as a subchannel TH component of VERA-CS. CTF includes a wide range of TH modules for LWR analysis (flow regime depending on two-phase wall heat transfer, inter-phase heat transfer and drag, droplet breakup, and quench-front search) and several internal models (spacer grid model, fuel rod conduction, use of steam-table as for the built-in material properties) to help facilitate the simulation of actual fuel assemblies. The code employs a two-fluid model (vapor and liquid) for analyzing two-phase flows considering three independent fluid fields (fluid film, fluid droplets, and vapor). Each of these fields is modeled with its own set of conservation equations (mass, momentum, and energy) using the Cartesian coordinate or simplified sub-channel approach. However, the liquid phase, both continuous and droplets, shares the same energy equation at thermal equilibrium, which implies that both fields have the same temperature for a given computational cell. Therefore, 8 equations in total need to be solved in CTF. Following are the conservation equations for the CTF two-fluid model:

1. Mass conservation

$$\frac{\partial}{\partial t}(\alpha_k \rho_k) + \nabla \cdot (\alpha_k \rho_k \vec{V}_k) = L_k + M_k^T \quad (4)$$

where the  $k$  subscript takes the following value: continuous liquid phase  $l$ , vapor phase  $v$ , entrained droplet phase  $e$ .

$LHS$  = change in mass over time

$L_k$  = mass transfer into or out of phase  $k$  (evaporation or condensation)

$M_k^T$  = mass transfer due to turbulent mixing and void drift

2. Momentum conservation: three momentum conservation equations are solved for the vapor, continuous liquid, and entrained liquid phase.

$$\begin{aligned} \frac{\partial}{\partial t}(\alpha_k \rho_k \vec{V}_k) + \frac{\partial}{\partial x}(\alpha_k \rho_k \mu_k \vec{V}_k) + \frac{\partial}{\partial y}(\alpha_k \rho_k \nu_k \vec{V}_k) + \frac{\partial}{\partial z}(\alpha_k \rho_k w_k \vec{V}_k) \\ = \alpha_k \rho_k \vec{g} - \alpha_k \nabla P + \nabla \cdot (\alpha_k \vec{\tau}_k^j) + \vec{M}_k^L + \vec{M}_k^d + \vec{M}_k^T \end{aligned} \quad (5)$$

where

$LHS1$  = volume momentum over time

$LHS2-4$  = mean advection of momentum in each of three Cartesian directions

$RHS1$  = gravitational force

$RHS2$  = pressure force

$RHS3$  = viscous share stress

$RHS4$  = momentum source term due to phase change and entrainment or de-entrainment

$RHS5$  = interfacial drag source term

$RHS6$  = momentum source caused by turbulent mixing and void drift.

3. Energy conservation: the energy conservations are solved for the vapor and liquid phases.

$$\frac{\partial}{\partial t}(\alpha_k \rho_k h_k) + \nabla \cdot (\alpha_k \rho_k h_k \vec{V}_k) = -\nabla \cdot (\alpha_k \vec{q}_k^T) + \Gamma_k h_k^i + q_{wk}^m + \alpha_k \frac{\partial P}{\partial t} \quad (6)$$

where

$LHS1$  = change of energy over time

$LHS2$  = advection of energy

$RHS1$  = inter-cell energy exchange due to void drift and turbulent mixing

$RHS2$  = volumetric wall heat transfer

$RHS3$  = fluid cell due to pressure

The use of the two-fluid model is useful in presenting high precision simulation for two-phase flows, which could occur in accident scenarios [32]. CTF features of the MPI based parallel algorithm, the boron tracking model and a developer-friendly coupling interface make CTF more practical and easier to be fully-coupled with other codes to improve accuracy and efficiency. The fuel conduction model to determine the temperature distribution of fuel rods of CTF is given below:

$$K_{UO_2,0.95} = 1.73035 \times \left[ \max \left( 1.1038 \frac{2.335 \times 10^3}{T_c + 464} \right) \right] + 7.027 \times 10^{-3} e^{1.8678 \times 10^{-3} T_c} \quad (7)$$

Another important feature of the CTF model is that it uses channel-centered geometry instead of rod-centered geometry normally used in the neutronic simulation as in TH1D and FRAPCON codes. Figure 4 shows the difference between the channels in the neutronics and CTF model. In MCS/CTF coupling, CTF receives the pin-wise power distribution to calculate the TH parameters used in MCS/TH1D. However, the fuel temperature, coolant temperature, and density calculated in CTF are not rod-centered as in the TH1D module. Therefore, to transfer the CTF data for use in MCS, the fuel pin temperature needs to be calculated from the surface average temperatures while the coolant temperature and density are calculated from the average of 4 sub-channels around the fuel pin [7] and can be expressed as follow:

$$T_{fuel} = \frac{1}{4}(T_{surface1} + T_{surface2} + T_{surface3} + T_{surface4})_{fuel} \quad (8)$$

$$T_{water} = \frac{1}{4}(T_{channelA} + T_{channelB} + T_{channelC} + T_{channelD})_{water} \quad (9)$$

$$\rho_{water} = \frac{1}{4}(\rho_{channelA} + \rho_{channelB} + \rho_{channelC} + \rho_{channelD})_{water} \quad (10)$$

Figure 5 illustrates the flow chart of MCS/CTF coupling, which quite similar to MCS/TH1D. After CTF receives the power profile from MCS, the 3D core information specified in MCS can generate an appropriate CTF input for the coupling simulation. For MPI parallel simulation, MCS uses the fuel assembly pre-processor to generate CTF input based on the information of each assembly with constant fuel gap conductance and independent fuel burnup of 10,000 W/m<sup>2</sup>-K, the same as in MCS/TH1D. The convergence criteria for the TH iteration in CTF is based on the five keys of global metrics associated with the solution at each iteration to reach steady invariant conditions within a user-specified tolerance.

The five global keys are:

1. The amount of energy stored in the flux

$$E_{solid,storage} = \frac{E_{rod} + E_{structure}}{Q_{rod} + Q_{fluid}} \cdot 100 \quad (11)$$

2. The amount of energy stored in the solids

$$E_{fluid,storage} = \frac{E_{fluid}}{Q_{rod} + Q_{fluid}} \cdot 100 \quad (12)$$

3. The amount of mass stored in the system

$$Mass_{storage} = \frac{Mass_{fluid}}{Mass_{inlet}} \cdot 100, Mass_{fluid} = \frac{1}{\Delta t} \sum_{cell=1}^{cells_{total}} \sum_{k=1}^3 |\alpha_k \rho_k - \alpha_k^o \rho_k^o| \quad (13)$$

4. The global energy balance

$$E_{global,balance} = \frac{Q_{rod} + Q_{fluid} + Q_{inlet} - Q_{outlet} - Q_{amb}}{Q_{rod} + Q_{fluid} + Q_{inlet}} \cdot 100 \quad (14)$$

5. The global mass balance

$$Mass_{global,balance} = \frac{Mass_{inlet} - Mass_{outlet}}{M_{inlet}} \cdot 100 \quad (15)$$

where

$Q_{rod}$  = power deposited into rods

$Q_{fluid}$  = power deposited into the coolant

$Q_{inlet}$  = energy coming in at the inlet of the model

$Q_{outlet}$  = energy leaving the system including energy leaving the outlet

$Q_{amb}$  = energy being lost to the environment

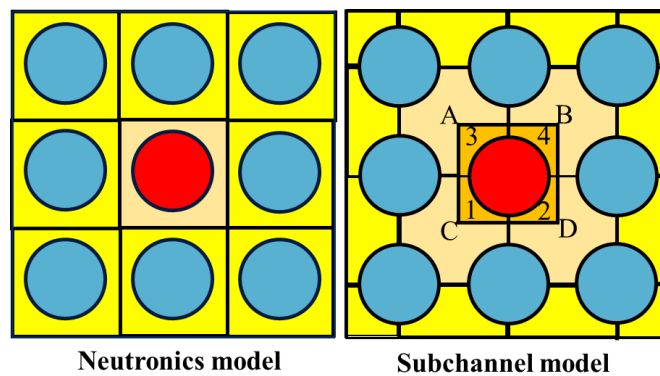


Figure 4. Neutronics and CTF subchannel model in MCS.

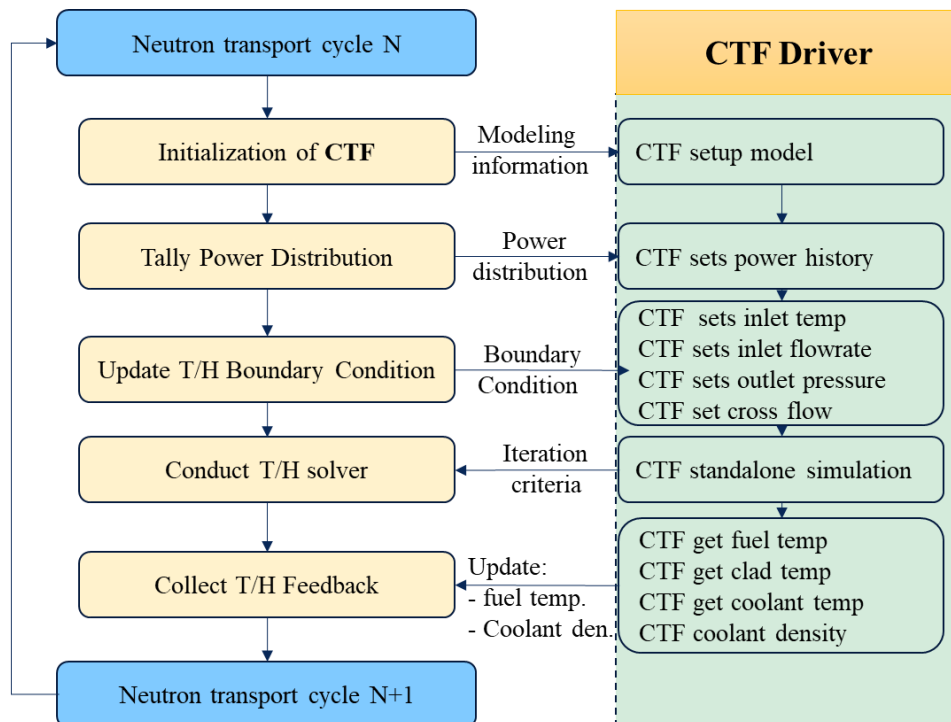


Figure 5. Flow chart of MCS/CTF coupling interface with Picard iteration methods.

### 2.2.3. MCS/FRAPCON Coupling

FRAPCON is an FP code developed by Pacific Northwest National Labs to calculate steady-state response for the thermal-mechanical behavior of oxide fuel rods behavior for long term and high burnups of up to 62 GWD/MTU of LWR core [33]. FRAPCON has been validated for different reactor core such as a boiling-, pressurized-, and heavy-water reactors. The code can accurately calculate and predict all significant fuel rod variables such as fuel and cladding temperature, fission gas release, pressure, deformation of the fuel rod, and cladding oxidation with the function of time-dependent fuel rod power and coolant boundary condition. FRAPCON model includes heat transfer between fuel-clad-coolant; fuel thermal expansion as fuel temperature-dependent; fuel thermal conductivity as a function of fuel temperature/density and burnup; solid mechanics, creep, corrosion, and single-channel thermal hydraulics. The code is a single channel and heat capacity dependent model that determines the coolant temperature as:

$$T_b(z) = T_{in} + \int_0^z \left[ \frac{(\pi D_0) q''(z)}{C_p G A_f} \right] dz \quad (16)$$

where

$$\begin{cases} T_b(z) & = \text{bulk coolant temperature at elevation } z \text{ on the rod axis (K)} \\ T_{in} & = \text{inlet coolant temperature (K)} \\ q''(z) & = \text{rod surface heat flux at elevation } z \text{ on the rod axis (W/m}^2\text{)} \\ C_p & = \text{heat capacity of the coolant (J/Kg} \cdot \text{K)} \\ G & = \text{coolant mass flux (Kg/s} \cdot \text{m}^2\text{)} \\ A_f & = \text{coolant channel flow rate (m}^2\text{)} \\ D_0 & = \text{outside cladding diameter (m)} \end{cases}$$

The radial temperature distribution in each fuel pin is calculated from the steady-state integral form of the heat conduction equation:

$$\iint_S k(T, \bar{x}) \vec{\nabla} T(\bar{x}) \cdot \vec{n} ds = \iiint_V S(\bar{x}) dV \quad (17)$$

where

$$\begin{cases} k & = \text{thermal conductivity (W/m} \cdot \text{K)} \\ s & = \text{surface of control volume (m}^2\text{)} \\ \vec{n} & = \text{surface normal unit vector} \\ S & = \text{internal heat source (W/m}^3\text{)} \\ T & = \text{temperature (K); } V = \text{control volume (m}^3\text{); } \bar{x} = \text{space coordinate (m)} \end{cases}$$

The fuel thermal conductivity is temperature and burnup-dependent with consideration of thermal expansion, irradiation swelling, and densification effects. Nuclear Fuel Industries (NFI) has developed the thermal conductivity model by applying only 95% of theoretical density oxide fuel (with or without gadolinium) based on the expression:

$$k_{UO_2,0.95} = \frac{1}{A + a \cdot gad + BT + f(Bu) + (1 - 0.9e^{-0.04Bu})g(Bu)h(T)} + \frac{E}{T^2} e^{-\frac{F}{T}} \quad (18)$$

where

$$\begin{cases}
 T = \text{temperature (K)} \\
 Bu = \text{burnup (GWd/MT)} \\
 f(Bu) = \text{effects of the product in fuel crystal matrix} \\
 \quad = 0.00187 \cdot Bu \\
 g(Bu) = \text{effects of irradiation defect} \\
 \quad = 0.038 \cdot Bu^{0.28} \\
 gad = \text{weight fraction of gadolinium} \\
 Q = \text{temperature dependent parameter} \\
 \quad = 6,380 \text{ (K)} \\
 h(T) = \text{temperature dependent annealing on radiation defects} \\
 \quad = \frac{1}{1 + 396 \cdot e^{-Q/T}} \\
 A = 0.0452 \text{ (m.K/W)}; B = 2.46 \times 10^{-4} \text{ (m/W)} \\
 E = 3.5 \times 10^9 \text{ (W} \cdot \text{K/m)}; F = 1,6361 \text{ (K)}; a = 1.1599
 \end{cases}$$

The fuel-cladding gap conductance is the total effect of three components: the conductance due to radiation, conduction through the gas, and conduction through regions of solid-solid contact, and is expressed as:

$$h_{gap} = h_{gas} + h_r + h_{solid} \quad (19)$$

1. Gas conductance

$$h_{gas} = \frac{k_{gas}}{\Delta x} \quad \text{where} \quad \begin{cases} k_{gas} = \text{gas thermal conductivity (W/m} \cdot \text{K)} \\ \Delta x = \text{total effect gap width} = d_{eff} + 1.8(g_f + g_c) - b + d \end{cases} \quad (20)$$

2. Radiation heat conductance

$$h_r = \sigma F_e F_a (T_f^2 + T_c^2)(T_f + T_c) \quad (21)$$

where

$$\sigma = \text{Stefan-Boltzmann const.} = 5.6697 \times 10^{-8} \text{ (W/m}^2 \cdot \text{K}^4)$$

$$F_e = \text{emissivity factor determined by routine EMSSF2}$$

$$F_a = \text{configuration factor} = 1.0$$

$$T_f = \text{temperature of fuel outer surface (K)}$$

$$T_c = \text{temperature of cladding inner surface (K)}$$

3. Solid-solid conductance

$$\begin{aligned}
 h_{solid} &= 0.4166 \cdot k_m \cdot P_{rel} \cdot R_{mult} / (R \cdot E) \quad \text{if } P_{rel} > 0.003 \\
 h_{solid} &= 0.00125 \cdot k_m / (R \cdot E) \quad \text{if } 0.003 > P_{rel} > 9 \times 10^{-6} \\
 h_{solid} &= 0.4166 \cdot k_m \cdot P_{rel}^{0.5} / (R \cdot E) \quad \text{if } P_{rel} < 9 \times 10^{-6}
 \end{aligned} \quad (22)$$

where

$$R_{mult} = 333.3 \cdot P_{rel} \quad \text{if } P_{rel} \leq 0.0087$$

$$= 2.9 \quad \text{if } P_{rel} > 0.0087$$

$$P_{rel} = \text{radio of interfacial pressure of cladding Meyer hardness}$$

$$k_m = \text{mean thermal conductivity of fuel and cladding (W/m}^2 \cdot \text{K)}$$

$$= 2K_f K_c / (K_f + K_c)$$

$$R = (R_f^2 + R_c^2)^{1/2} : \text{roughness}$$

$$E = \exp\left[5.738 - 0.528 \cdot \ln(R_f \cdot 3.937 \times 10^{-7})\right]$$

In the MCS/FRAPCON coupling system, FRAPCON receives the power distribution and the burnup interval from MCS at each time step. The FRAPCON is then treated as an FP solver for the MCS code by calculating: 1) temperature of the fuel and cladding, 2) fuel and cladding deformation, 3) fission product generation and release, void volume, and fuel rod internal gas pressure. Since FRAPCON is a pin-cell solver similar to TH1D, the data exchange in the MCS/FRAPCON coupling system is accomplished by the Pin-wise Data Transfer Scheme (PDTS). FRAPCON determines the fuel rod response for each time step and provides detailed information of the fuel/coolant temperature, coolant density, gap conductance, thermal conductivity, cladding hoop stresses and strains, gap size, gap conductance, and oxide layer thickness. The calculated values are then updated into the MCS. The flow chart of the MCS/FRAPCON coupling interface is shown in Figure 6. A study by Ju. [15] proved that differences in the coolant temperature distribution of the three MCS couplings cause the different versions of the steam table employed in each solver. To reduce the discrepancy caused by the different steam table, MCS, therefore, adapts the same IAWPs steam table for all MP solvers. Table 1 summarizes the mechanism of each computation code: TH1D, CTF, and FRAPCON. The highlighted blue color refers to the advantages of one compared to another.

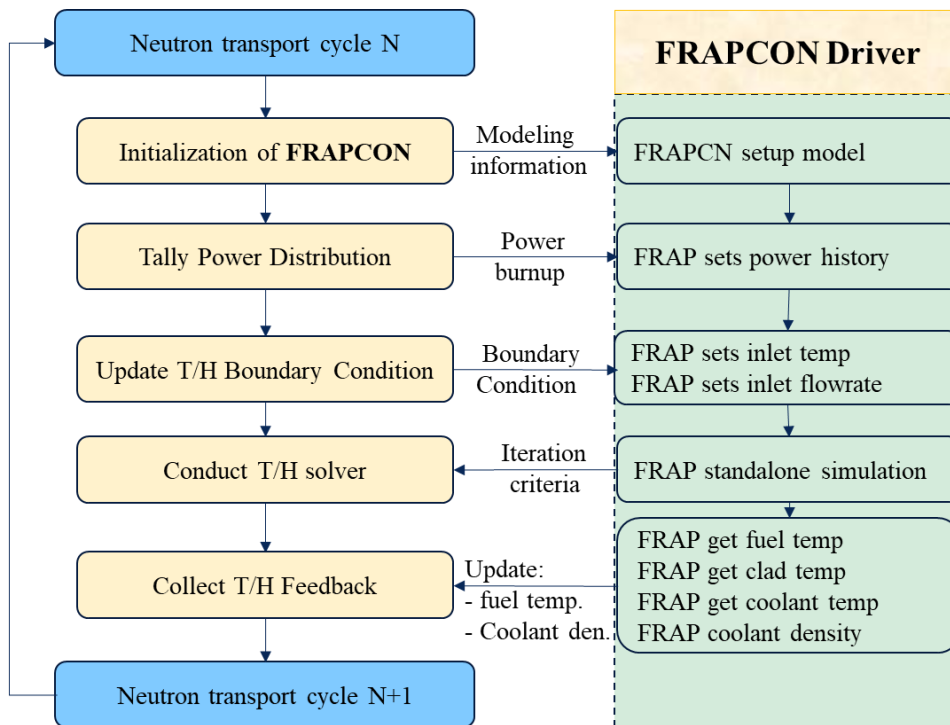


**Figure 6. Flow chart of the MCS/FRAPCON coupling interface.**



**Table 1. The comparison of computation code for MCS couplings.**

	<b>TH1D</b>	<b>CTF</b>	<b>FRAPCON</b>
<b>Conservation Equations</b>	Mass and energy for 1D axial direction (2)	Mass, energy, and momentum (axial and transverse linear) (8)	Mass and energy for 1D axial direction (2)
<b>Two-phase model</b>	No, a single 1D model	Yes, three field model (fluid film, fluid drops, and vapor)	No, a single 1D model
<b>Cross-flow model</b>	No, closed coolant channel	Yes, open coolant channel	No, closed coolant channel
<b>Conduction model</b>	User-defined gap conductance	User-defined gap conductance	Detailed modeling - Deformation, fission gas release model - Dynamic gap conductance
<b>Calculation unit</b>	Pin-wise	Pin-wise	Pin-wise
<b>Parallel simulation</b>	Yes.	MPI available in the unit of assembly	Yes.
<b>Other features</b>	None.	DNBR, Boron tracking, coupling interface for neutronic code	Burnup dependent, burnup calculation,
<b>Computing cost</b>	Not expensive	Expensive	Expensive

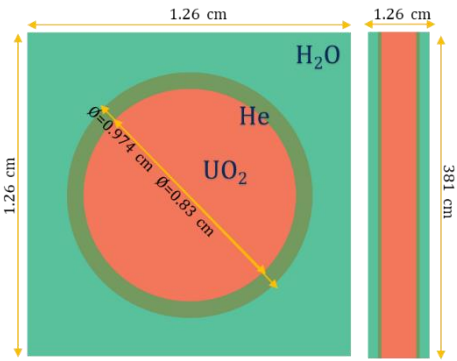
### III. Verification and Validation of MCS Multi-physics Coupling Model

The study of the MCS MP couplings was conducted for a 3D MP framework to evaluate the behavior of coolant and fuel systems, from pin-cell level, and to multi-pin (assembly) and multi-assemblies model from the OPR-1000 core. The verification and validation of MCS MP systems are then conducted for the OPR-1000 full core problem, and their results compared against the NDR, STREAM/RASTK2 code, STREAM-3D code, and measured data.

#### 3.1. Fuel pin model

The pellet, cladding, and coolant are explicitly modeled and divided axially into 44 meshes. The details of pin-cell parameters are listed in Table 2 with the image of the top and side view generated in the MCS plot.

**Table 2. Pin model in MCS and parameters.**

	Parameter	Value
	Pellet radius (cm)	0.41553
	Clad inner radius (cm)	0.42244
	Clad outer radius (cm)	0.48609
	Pin pitch (cm)	1.26
	<sup>235</sup> U enrichment (wt.%)	1.42
	Active height (cm)	381
	Axial meshes (#)	44
	Moderator density (g/cm <sup>3</sup> )	0.7
	Material temperature (K)	293.6
	Pin power (MW)	0.083468
	Flow rate (kg/s)	0.335276

### 3.2. 16x16 assembly and 2x2 core model

Each fuel assembly in OPR-1000 consists of a 16x16 array of 235 fuel rods and 5 guides. The guide tube size is equal to four fuel rods position for providing channel with control element assembly (CEA) movement during the operation. The fuel assembly with a slightly enriched UO<sub>2</sub> rod and Gd<sub>2</sub>O<sub>3</sub> rod is studied for the comparison of the three MCS coupled systems. Each fuel pin in this study is divided unequally into 44 meshes in the axial direction, and each spacer grid location is counted as 1 axial mesh. Each fuel pellet that contains the gadolinium is sub-divided into 10 radial rings to better simulate the strong spatial self-shielding and large absorption rates, whereas the UO<sub>2</sub> fuel pins are not subdivided radially. Figure 7 shows the details of the assembly (left) and 2x2 checkboard core generated in the MCS model.

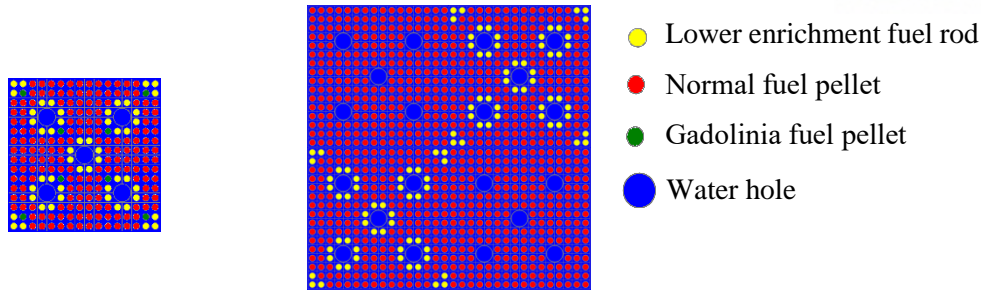


Figure 7. 16x16 OPR fuel assembly (left) and 2x2 checkboard core (right).

### 3.3. OPR-1000 core

The OPR-1000 core consists of 177 fuel assemblies loaded in a 15x15 array in the core with a total thermal power of 2815 MWth. Cycle 1 employs Guardian type assembly, while Cycle 2 employs the PLUS7 type assembly, which has different axial space grid locations and fuel pellet diameters [5]. The typical spacer grid of PWR, which has Inconel at the bottom, and nine grid in the axial direction are implicitly modeled. The fuel materials utilize slightly enriched uranium dioxide ( $\text{UO}_2$ ) pellets with  $^{235}\text{U}$  enrichment ranging from 1.7 to 4.7 wt%. Some fuel rods present an axial cutback and blanket regions depending on location in the core. The burnable neutron absorber is the gadolinia ( $\text{Gd}_2\text{O}_3$ ) with 6-8 w/o, admixed in enriched  $\text{UO}_2$ .

A 3D one-fourth of the OPR-1000 full core is developed for MCS with other components of the full core such as baffle, barrel, and reactor vessel. In the conventional neutronic calculation, these components are usually neglected or approximated due to low neutron flux at the reflector region. However, Ryu [30] shows their non-negligible effect on the power distribution at the corner of the assembly, which also requires implicit modeling. The OPR-1000 quarter-core pin-wise depletion for three consecutive cycles is conducted with the developed MCS MP systems along with three other feedback kernels such as depletion, TH feedback, equilibrium xenon update, and CBC search. Figure 8 shows the quarter OPR core loading pattern for Cycles 1 and 2.

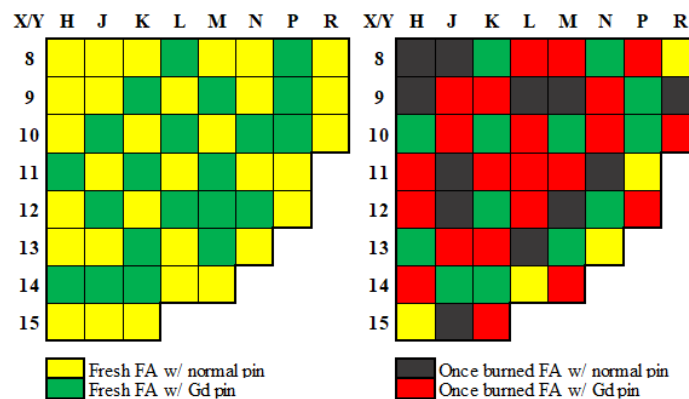


Figure 8. Loading patterns of Cycle 1 (left) and Cycle 2 (right).

### **3.4. Code for comparison**

#### **3.4.1. *STREAM/RASTK2 (ST/R2)***

STREAM/RAST-K2.0 (ST/R2), composed of STREAM, STORA, and RAST-K2.0, is a conventional deterministic two-step approach coding system for LWR core design and analysis. It is developed by the UNIST CORE group and consists of the lattice transport code STREAM and the nodal diffusion code RAST-K 2.0. STREAM is a 2D lattice neutron transport analysis code using the Method of Characteristics (MOC) to solve the transport equation. It can solve the complicated radial geometries composed of fuel pin, burnable absorber, and structural material. STREAM generates fuel assembly and reflector constants for further use in RAST-K 2.0 whole-core simulation. STORA (STREAM TO RAST-K 2.0) converts the STREAM data set and compile it into a library to use in RAST-K2.0. RAST-K 2.0 solves the 3-D two-group steady and transient diffusion equations by applying the unified nodal method (UNM) and apply for the whole-core simulation. ST/R2 has been validated and verified in an earlier study [34] for OPR1000 and APR1400.

#### **3.4.2. *STREAM-3D (ST3D)***

STREAM has also adapted a 3D method of characteristics/diamond-difference (MOC/DD) for the direct whole-core analysis to enhance accuracy and eliminate the uses of approximations in the conventional two-step method [35]. STREAM3D has been validated and verified in an earlier study [36] for OPR1000 and APR1400.

#### **3.4.3. *Nuclear Design code***

The nuclear design and analysis of OPR-1000 summarized in the nuclear design report (NDR) were based on the 3D diffusion theory calculation for the entire core, which employs the cross-section generated by the 2D transport theory calculation for each fuel assembly. The two-step method used for the OPR-1000 core system is DIT/ROCS in Cycle 1 and PARAGON/ANC in Cycle 2.

## **IV. Verification and validation of the MCS MP coupling system**

### **4.1. Fuel pin**

In this simulation, 10 inactive and 40 active multi-cycles are simulated; each multi-cycle has 200 single cycles to ensure fission source distribution convergence with 10,000 histories in each cycle. Therefore, two million histories were employed in each cycle on a Linux cluster with 56 processes (Intel

Xeon E5-2620 @ 3.00 GHz). The simulation is performed at hot full power (HFP), assuming that all materials are at room temperature. The pin power and flow rate in Table 2 are calculated by dividing the total number of pins in the whole core from the total core power and flow rate, respectively.

Table 3 compares the MCS neutron transport calculation results with the MCS coupled systems (TH or FP code). The calculated CBC of MCS without MP coupling is larger compared to the MCS coupled code system, due to the feedback effect from the coolant and fuel being ignored which prove the need for neutronics and TH/FP coupling. The calculated CBC values of all MCS MP couplings have a difference of less than 1 ppm. As shown in Table 3, the MP solver simulation time per cycle of TH1D is very short compared to FRAPCON and CTF, because only 2 conservational equation needed to be solved in TH1D. In comparison, CTF needs to solve 8 conservational equation in each cycle for the sub-channel simulation. Even though FRAPCON solves only 2 conversational equations in 1D as in TH1D, but the dynamic gap conductance and thermal conductivity need to be calculated in every iteration, which increases the simulation time. However, the total execution time for CTF is similar to TH1D because a single pin model in the CTF has only four sub-channels and need not consider the cross-flow effect form the neighboring pins. Similarly, the execution time for FRAPCON is also similar to TH1D because the calculation is performed only at the beginning of the cycle (BOC) without the burnup step information. Figure 9 shows the axial power distribution of the three coupled systems, which agree well with the maximum relative difference of less than 3%. The ten small deeps, corresponding with the ten spacer grid locations in the active fuel region, are observed in the axial power and fuel temperature distributions. The calculated fuel temperature distribution shows a significant difference in the FRAPCON model and has the highest fuel temperature value compared to those in TH1D and CTF. The discrepancies in the thermal conductivities calculation and the use of dynamic gap conductance in FRAPCON solver [13] affect the fuel temperature calculation, as shown in Eqs. (18) and (19), while the TH1D and CTF solver employed the constant gap conductance. Figure 10 shows that the modified gap conductance in the FRACON solver to be constant at  $10,000 \text{ W/m}^2\text{-K}$  to produce similar fuel temperature distribution as TH1D and CTF. Another noticeable result is that the calculated fuel temperature distribution in FRAPCON does not show large deep at spacer grid location as in TH1D and CTF since high-fidelity FP parameters such as thermal fuel expansion and fission gas release are considered in the FRAPCON model. The moderator temperature and density distribution of each coupled system confirm high agreement, as shown in Figure 9. In contrast, the calculated outlet temperature, which will be used for updating the temperature in the next depletion step of the coupled systems, does not show significant differences from each other.

**Table 3. Summary of calculated pin results.**

	No-MP	TH1D	CTF	FRAPCON	FRAPCON Hgap= 10,000
Execution time (core-h)	31.7	32.1	35.1	32.4	32.3
Solver time (s)	-	0	2.08	0.14	0.14
CBC (ppm)	875.2 ± 1	874.5 ± 1	874.8 ± 1	874.5 ± 1	875.1 ± 1
Max rel. pow. dif. (%)	-	-	3.0 ± 3.3	0.9 ± 1.6	1.1 ± 4.5
Min rel. pow. dif. (%)	-	-	4.5 ± 5.0	1.7 ± 4.1	2.3 ± 5.4
Outlet temp. (K)	-	599.12	599.11	598.98	599.0
Max. fuel temp. (K)	-	1366.9	1362.7	1432.7	1382.3
Solver simulation time* = average MP solver simulation time per cycle					

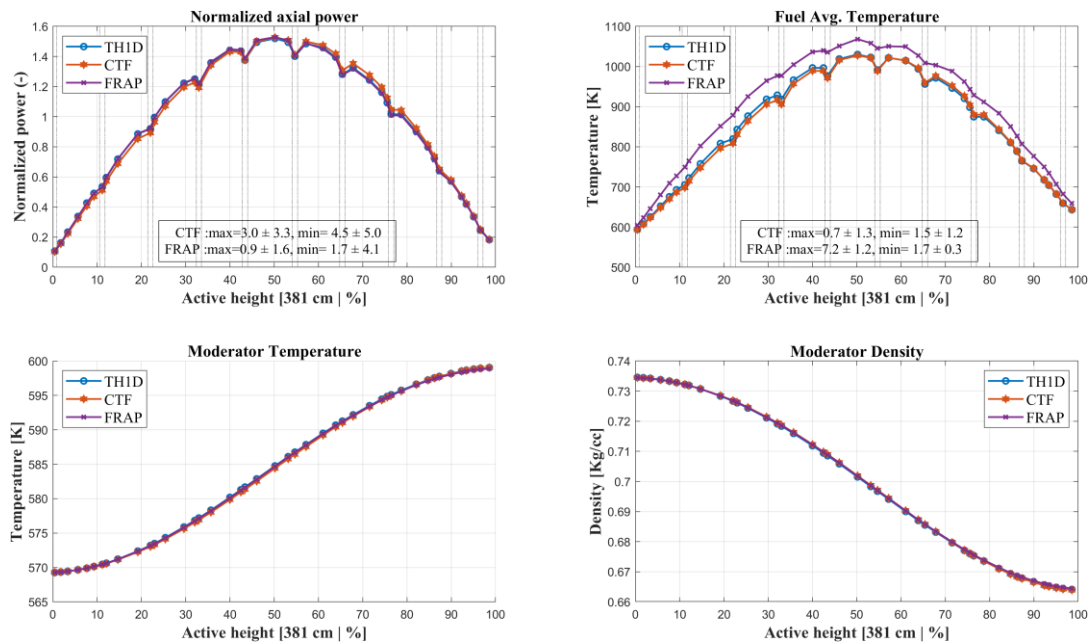


**Figure 9. Comparison of pin test results of axial power, fuel temp, coolant temperature and density of MCS multi-physics couplings.**

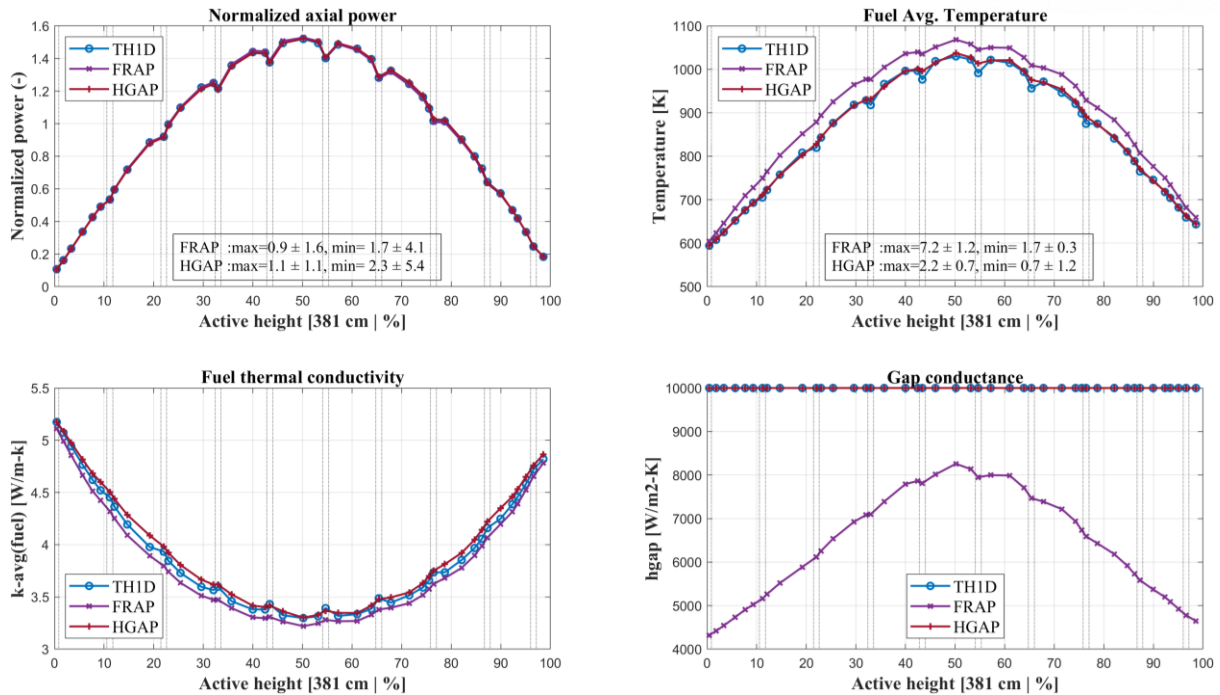


**Figure 10. Comparison of pin test results of axial power, fuel temp, coolant temp. and density of MCS multi-physics couplings with constant gap-conductance in FRAPCON.**

#### 4.2. 16x16 assembly

A 16x16 array assembly from the OPR-1000 reactor core consisting of pins with and without gadolinium is tested. The simulations were performed with 50 active cycles, 10 inactive cycles with 200 sub-cycle and 10,000 histories per cycle to achieve CBC with around 1 ppm standard deviation. Table 4 shows a similar trend as results in pin cell problems despite the CTF solver simulation time per cycle and total execution time being much longer than in TH1D and FRAPCON. The CTF solver simulation time is 332 s per cycle, which is 600 and infinite times longer than in FRAPCON and TH1D, respectively, because CTF does not require parallel processing for single assembly calculation. Even though 84 processors are used in these simulations, only 1 processor is used during the CTF stand-alone simulation, while TH1D and FRAPCON run parallel with 84 processors. However, the 16x16 fuel assembly (236 fuel pins, 5 guide tubes located in 25 fuel pins) will consider the 289 sub-channels while calculating the TH parameters in the CTF model, which will increase the simulation time. Figure 11 shows that the higher coolant temperature and lower coolant density at the top of active core height in MCS/CTF compared to MCS/TH1D and MCS/FRAPCON, due to the effect of sub-channel model in CTF. Figure 12 shows the pin-wise power, fuel average temperature, coolant temperature, and density distribution of the three MCS coupled systems. The calculation results from the TH1D module are used as a reference, and the differences compared to CTF and FRAPCON are shown in Figure 13. Overall, the pin-wise power and average fuel temperature distribution of the three modules show similar



distribution trends. However, the calculated fuel temperature in the FRAPCON module has a large discrepancy, within 47 K, against the TH1D module, which, as mentioned earlier, is caused by considering the dynamic gap conductance and thermal conductivity in the FRAPCON model. The maximum difference of calculated fuel temperature in the CTF and TH1D module is at the gadolinium pin having the low power because CTF calculated the fuel temperature as an average of 4 fuel pins surface value and the CTF neighboring sub-channels have a higher temperature than in gadolinium pin, while TH1D does not. The coolant temperature and density distribution results of the three modules show that the CTF has a more realistic distribution (smooth distribution) than TH1D and FRAPCON (discretized distribution). The differences are caused by considering the cross-flow in which the fuel and coolant temperatures are calculated by averaging the results from adjacent sub-channel in the CTF model while TH1D and FRAPCON use the closed channel model that does not consider heat exchange between the neighboring channels.

**Table 4. Summary of the calculated results of the fuel assembly test.**

	<b>No MP</b>	<b>TH1D</b>	<b>CTF</b>	<b>FRAPCON</b>
Execution time (core-h)	36.6	38.5	504.3	39.2
Solver time (s)	-	0.0	332.6 ± 31.3	0.5 ± 0.005
CBC [ppm]	1873.3 ± 0.8	1872.0 ± 0.9	1873.1 ± 0.8	1872.5 ± 0.8
Max rel. pow. dif. (%)	-	-	2.5 ± 4.2	5.2 ± 4.4
Min rel. pow. dif. (%)	-	-	3.5 ± 5.4	2.2 ± 2.1
Outlet temp. (K)	-	599.02	598.87	599.56
Max. fuel temp. (K)	-	1274.5	1262.9	1313.9



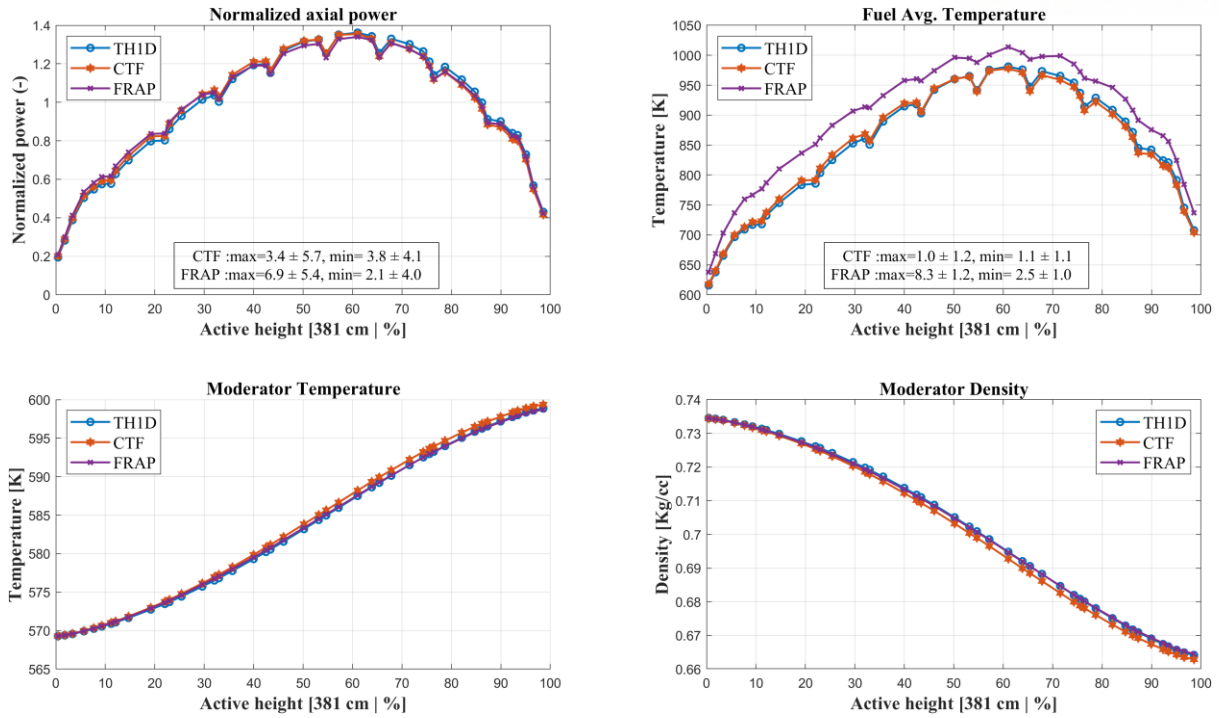


Figure 11. Axially integrated results of a fuel assembly in MCS coupling.

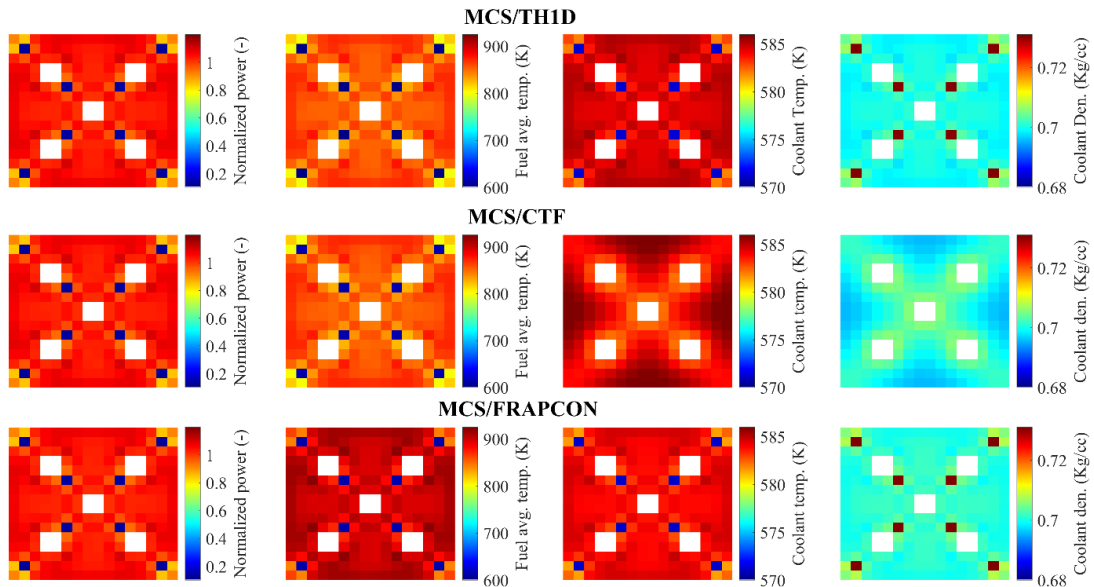
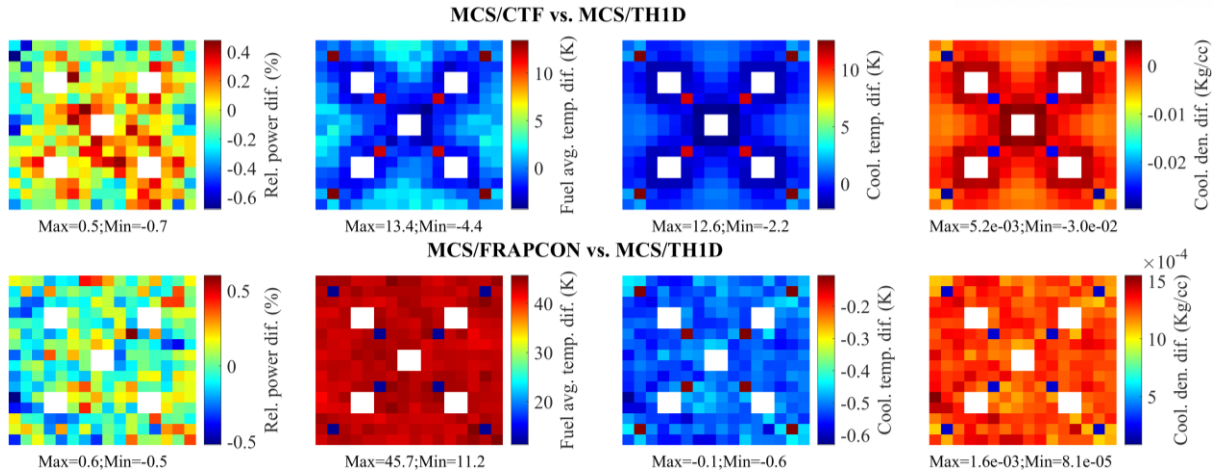


Figure 12. Pin-wise distribution in fuel assembly problem of MCS coupled systems.



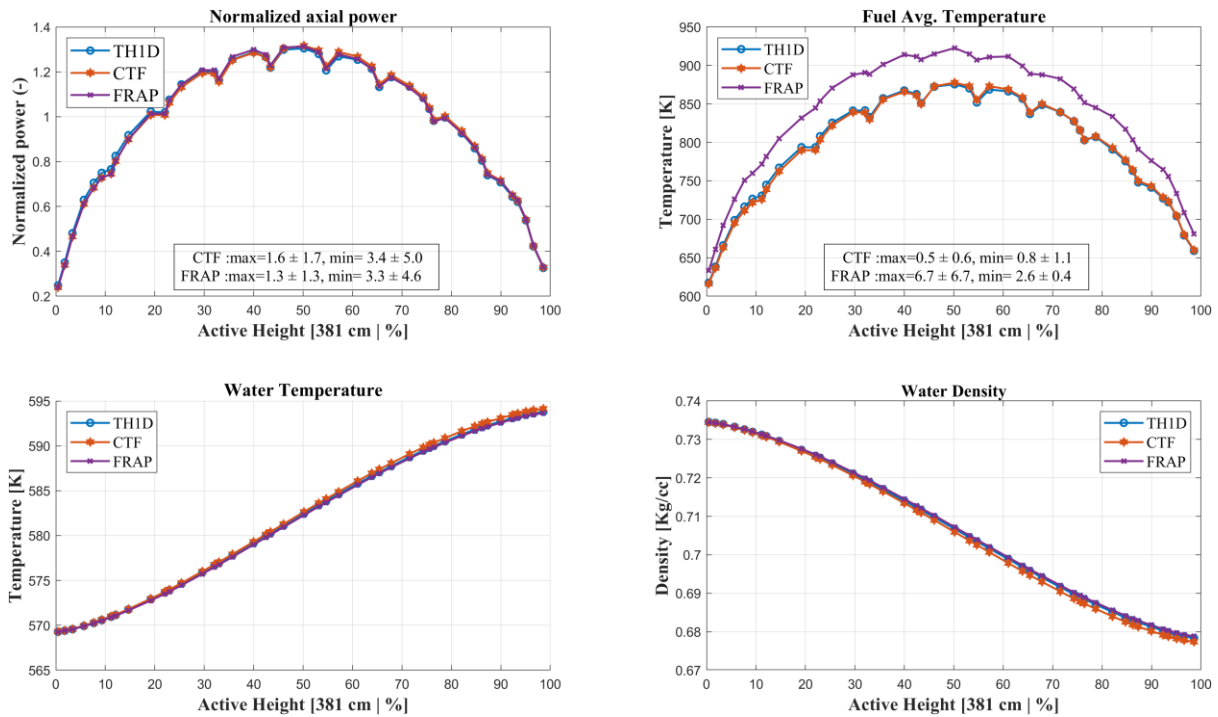
**Figure 13. MCS/CTF and MCS/FARAPCON pin-wise distribution differences compared to MCS/TH1D.**

### 4.3. Checkboard 2x2 assemblies

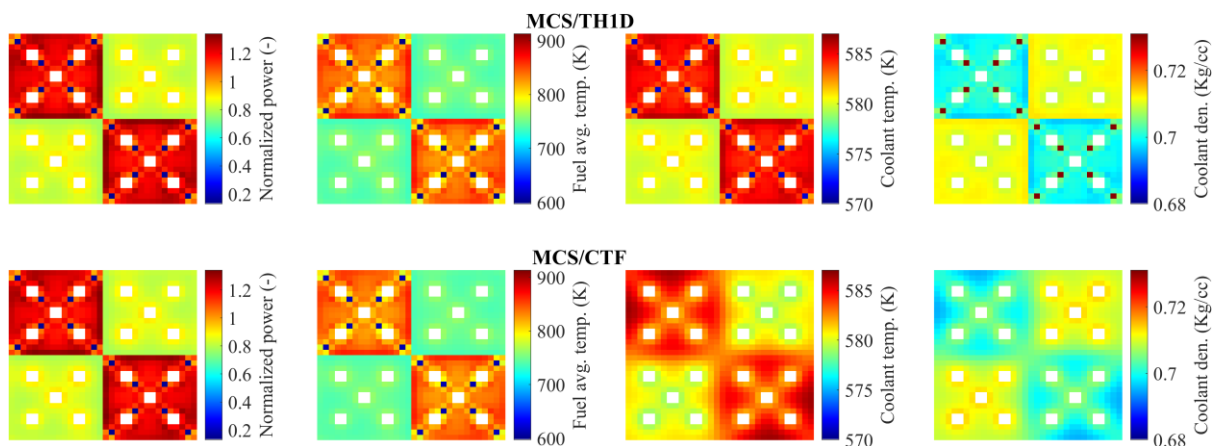
The checkboard 2x2 assemblies simulation is performed with 20 active cycles, 5 inactive cycles with 300 sub-cycles, and 20,000 histories per cycle. Table 5 summarizes the results for the CBC, relative power difference, and outlet temperature; Figure 14 illustrates the axial distribution results of the three modules, which show no significant difference from the results in the assembly problem. The CTF solver simulation time in this 2x2 checkboard core (total 4 assemblies) has a similar time as in an assembly problem because the CTF parallelization can be used within the assembly unit by generating new input for each assembly and performing their simulation separately. For the TH1D and FRAPCON solver, the number of simulations are increased because more depletion cells need to be calculated. For the axial average power distribution, the three MCS coupled systems have a slight difference between 1.3% to 3.4% within 2 statistic standard deviation. Figure 15, which illustrates the axially integrated pin-wise distribution results from the three modules, shows that the borders of the assemblies have a high-temperature gradient due to the different power of the assemblies. For TH1D and FRAPCON solver, which do not consider the cross-flow effect from the coolant in the adjacent assembly border, the borders in the high power region has a higher temperature, whereas lower temperatures will be obtained at the low power regions. In CTF, the coolant temperature and density at assembly boundaries are flatter, and the highest distribution is no longer at the assembly boundary. However, the overall difference between each calculated result is not significant. Figure 16 illustrates the difference in power, temperature, and density of MCS couplings. It shows that the fuel and coolant temperature distribution in MCS/CTF has large discrepancies at low power pin (at gadolinium pin location as in one assembly problem) and boundaries of high and low power assembly if compared to MCS/TH1D results.

**Table 5. Summary of MCS calculated results for 2x2 core.**

	TH1D	CTF	FRAPCON
Execution time (core-h)	85.0	276.3	87.0
Solver time (s)	0.03±0.0	328.5±75.6	1.75±0.006
CBC [ppm]	1054.6±0.9	1056.5±0.6	1056.5±0.8
Max rel. pow. dif. (%)	-	1.6±1.7	1.3±5.2
Min rel. pow. dif. (%)	-	3.4±5.0	3.3±4.6
Outlet temp. (K)	593.89	594.22	593.75
Max. fuel temp. (K)	1083.6	1082.4	1140.9



**Figure 14. Axially integrated results of 2x2 core in MCS couplings.**



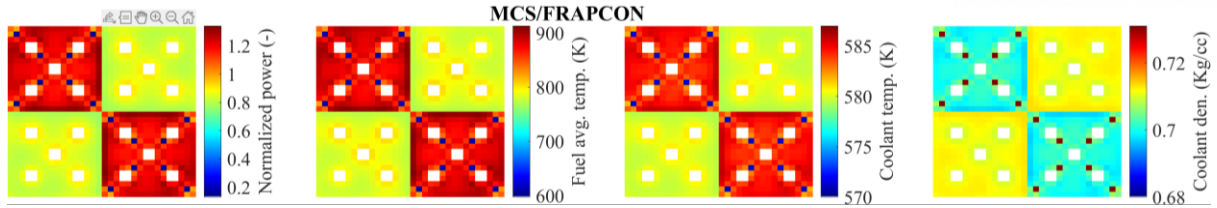


Figure 15. Pin-wise distribution of checkboard 2x2 core in MCS coupled systems.

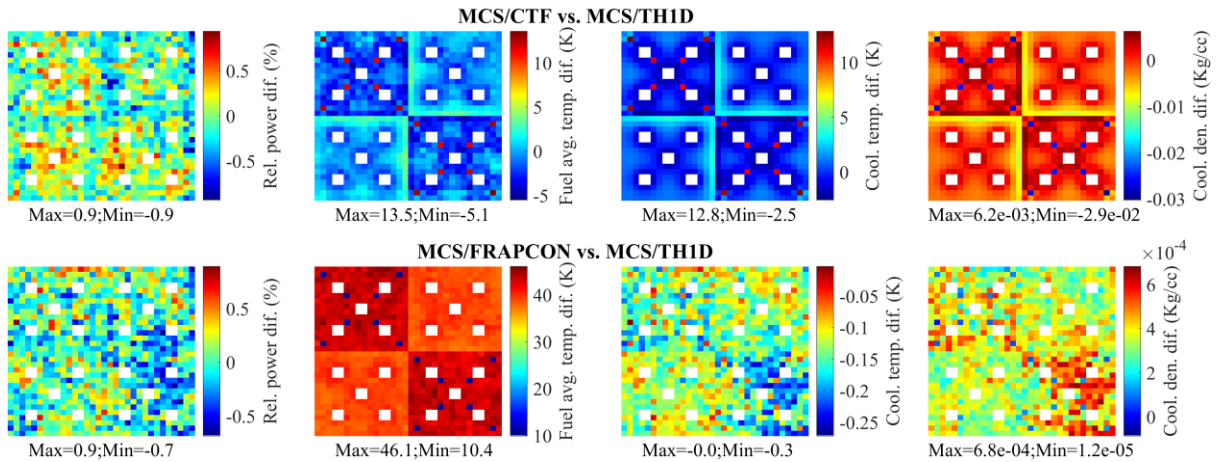


Figure 16. MCS/CTF and MCS/FARAPCON pin-wise differences compared to MCS/TH1D.

#### 4.4. Multi-physics full core results

Overall, the HFP quarter-core depletion in MCS calculation of the OPR-1000 is simulated with the ENDF/B-VII.1 library. Each transport step includes 4 inactive cycles, 20 active cycles, 200 sub-cycles, and 10,000 neutron histories per sub-cycle (that is, 2 million neutron histories per cycle, 48 million neutron histories per transport step, and about 5 neutron histories on average per cycle per depletion cell) giving the statistical uncertainty of the multiplication factor  $k_{\text{eff}}$  to be less than 15 pcm and CBC to be less than 2.5 ppm.

##### 4.4.1. The Zero Power Physics Testing verification

The Zero Power Physics Testing (ZPPT) verifies the nuclear design and robustness for reactor safety. The ZPPT was conducted at the beginning of the reactor's life, in hot zero power (HZP) condition without xenon at a temperature of 296.11 °C and pressure of 158.18 bars. Measured data for the ZPPT is not provided. Therefore, the verification of MCS is done against the data obtained from NDR and ST/R2 calculations. The OPR-1000 core contains 73 control element drive mechanisms (CEDMs) defined into five regulating and two shutdown groups made of B<sub>4</sub>C pellets and one part-strength group made of Inconel pellets. The verification of the five control element assemblies (CEAs) regulating group

calculated with MCS, and MCS solutions against NDR and ST/R2 are summarized in Figure 17. The exact NDR data values are not shown for confidentiality reasons. No analysis of the power coefficient is conducted because the information necessary to compute them (control rod positions and boron concentration) is not provided. MCS predicts a CBC value of 1,081 ppm for All Rod Out (ARO) state, a difference of only 4 ppm compared to ST/R2 CBC results. The CEA group worth validated by MCS shows maximum relative differences of ~9% compared to NDR and -4.4% compared to ST/R2.

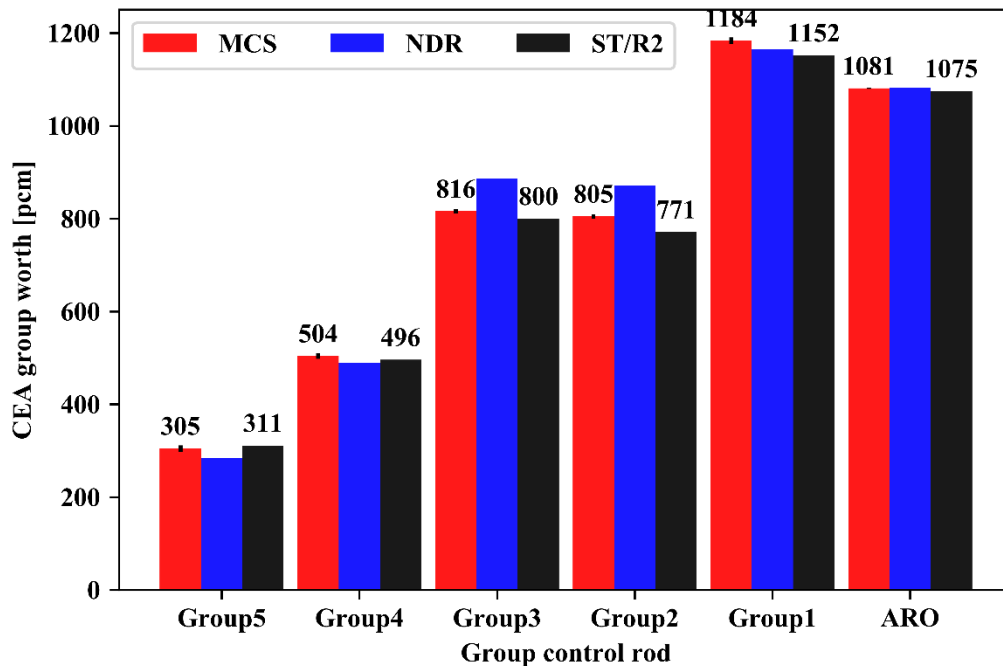


**Figure 17. Verification of ZPPT at the beginning of reactor life (BOC, HZP, no Xe).**

#### 4.4.2. MCS/TH1D cycle01

The good agreement found between the MCS model and the NDR and ST/R2 results for the ZPPT application allows for HFP steady-state depletion of the OPR-1000 system for the verification and validation (V&V) of MCS coupling capability and accuracy. The study of MCS pin-wise depletion simulation is coupled with TH1D solver considering the following feedbacks during the whole-core depletion calculation: equilibrium xenon, T/H feedback, CBC search, and OTF cross-section reconstruction with ENDF/B-VII.1 combined with the JENDL4.0 cross-section. A semi predictor-corrector depletion algorithm, with a specific quadratic scheme for the depletion of gadolinia pins, is applied. The number of computing fuel cells of quarter-core of OPR-1000 Cycle 1 was 535,524 with non-uniform height of 44 axial meshes (normal fuel cells = 10,251 pins x 44 axial meshes x 1 radial ring = 451,044 cells, gadolinium fuel cells = 192 pins x 44 axial meshes x 10 radial rings = 84,480 cells). Each transport step includes 5 inactive cycles, 20 active cycles, 300 sub-cycles, and 20,000

neutron histories per sub-cycle (that is, 6 million neutron histories per cycle, 120 million neutron histories per transport step, and about 11 neutron histories on average per cycle per depletion cell). The simulation time for Cycle 1 with 31 burnup steps (totaling 13.987 GWD/MTU) on 72 CPUs of “2.8 GHz, Intel (R) Xeon (R) CPU” is approximately 14,250 core h (~198 h wall clock time). The memory usage reaches about 18 GB per processor when the number of isotopes in depletion fuel cells gets saturated. The depletion of boron concentration in the moderator/coolant is not modeled. MCS/TH1D simulation takes around 5 h with 72 processors at EOC for one transport and one burnup step.

Figure 18 displays the boron letdown curves and axial shape index (ASI) of MCS compared to the measured data (notice that no measured data is available at BOC); results obtained from NDR, ST/R2, and ST3D and the summary of V&V error are shown in Table 6. The MCS average standard deviation of CBC is 1 ppm. The calculated CBC of MCS underestimates the measured data with a maximum difference of around 44 ppm ( $1\sigma = 1$  ppm) at 6 GWD/MTU. At the end-of-cycle (EOC), the CBC difference between MCS and measured data is 13 ppm, which is relatively small, illustrating the MCS capability to predict the gadolinium depletion behavior and the cycle length in OPR-1000. MCS predicts CBC within 33 ppm, 25 ppm, and 16 ppm compared to the NDR data, ST/R2, and ST3D solutions, respectively. Figure 18 (right side) displays a similar trend of calculated ASI of MCS compared to all references. Figure 19-Figure 24 show the normalized radial assembly-power profile of MCS and the relative difference compared to reference at BOC (0.05 GWD/MT), MOC (6.0 GWD/MT), and EOC (13.8 GWD/MT); and the normalized axial power distribution of MCS compared with the references. The parameter at each height has been radially integrated across the core. A synthesis of measured radial and axial power profiles is obtained by using in-core detector signals located in the assemblies through the CECOR code: the corresponding exact values are confidential and cannot be disclosed in this paper. The relative errors for the axial profiles are not computed due to the differences in axial mesh size of the MCS model and the references. Table 7 summarizes the relative differences in the power and RMS errors in MCS compared to references. Good agreement is observed between MCS and the references with a maximum RMS error of less than 1.8% throughout all states. Larger discrepancies between MCS and measured data in relative assembly power occurs in the core-periphery where the power is relatively low, with the statistical uncertainty around 2.4% at the edge within 1 standard deviation and the average statistical uncertainty of 0.9% at EOC as shown in Figure 25. Figure 25 presents the axially integrated relative pin-power profile and the relative statistical uncertainty of MCS at BOC and EOC. The power distribution becomes flattered as the burnup increases with decreasing peak power at BOC compared to EOC. The axial profiles of fuel pin temperature and moderator temperature/density calculated by MCS are illustrated in Figure 26, and MCS results compared against ST/R2 are shown in Figure 27 (the measured and NDR data are not available for those quantities).



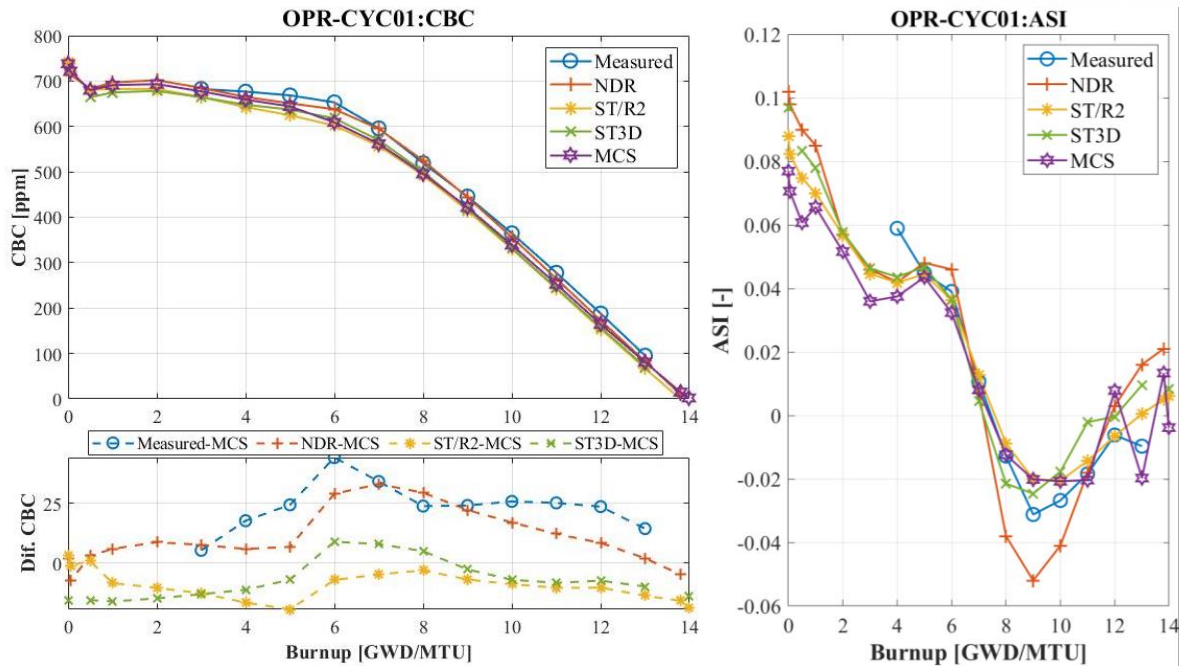


Figure 18. MCS/TH1D V&V of boron letdown curve and ASI results.

Table 6. Summary of MCS V&V error statistics for OPR-1000.

	CBC dif. [ppm] <sup>b</sup>				ASI dif. [-] <sup>b</sup>			
	M <sup>a</sup>	NDR	ST/R2	ST3D	M <sup>a</sup>	NDR	ST/R2	ST3D
<b>Mean</b>	-23.83	9.87	-9.16	-7.59	-0.001	0.006	0.005	0.008
<b>STD</b>	9.51	11.50	6.34	8.05	0.010	0.018	0.008	0.011
<b>Max.</b>	-5.28	33.01	3.35	8.87	0.014	0.036	0.020	0.029
<b>Min.</b>	-44.12	-7.57	-19.44	-16.15	-0.021	-0.032	-0.014	-0.009
<b>RMS</b>	25.66	15.16	11.14	11.06	0.010	0.019	0.009	0.013
<sup>a</sup> Measured								
<sup>b</sup> Measured (or NDR, ST/R2, ST3D) – MCS;								

Table 7. Summary of relative error in radial assembly power distribution.

	BOC (0.05 MWD/MT)			MOC (6.0 MWD/MT)			EOC (13.8 MWD/MT)		
	Max.	Min.	RMS	Max.	Min.	RMS	Max.	Min.	RMS
M.	-	-	-	3.56	-2.27	1.62	5.20	-1.60	1.45
NDR	2.11	-4.35	1.61	2.48	-5.20	1.77	1.88	-5.12	1.78
ST/R2	1.02	-1.43	0.61	0.51	-0.67	0.34	0.70	-0.74	0.36
ST3D	1.46	-2.29	1.02	1.97	-2.64	1.14	1.60	-1.45	0.71
Relative error = 100*(MCS/M - 1)									

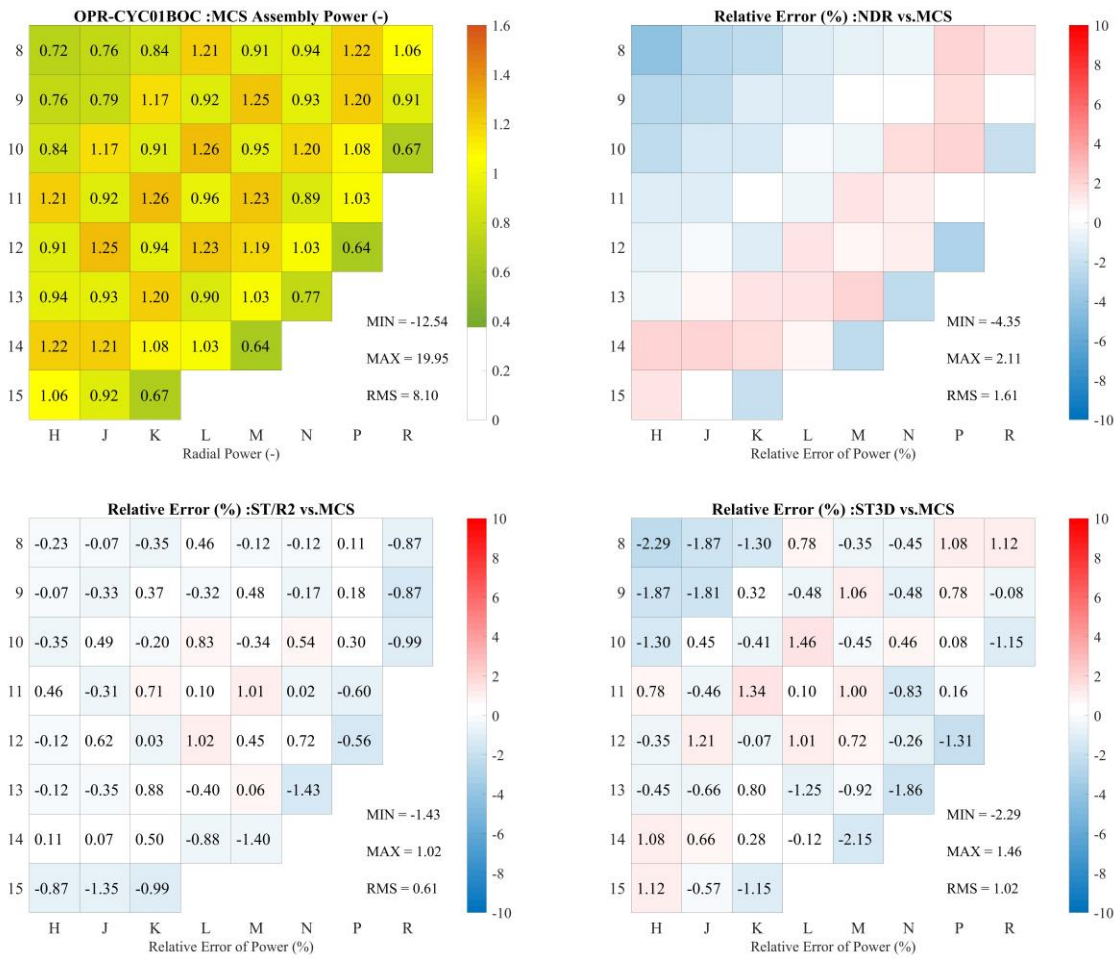


Figure 19. MCS radial assembly power distribution and relative error at BOC Cycle 01.

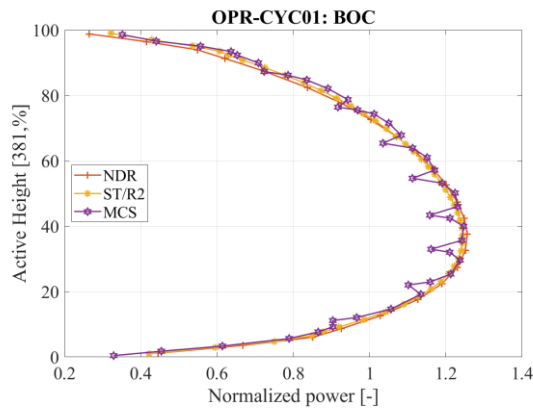
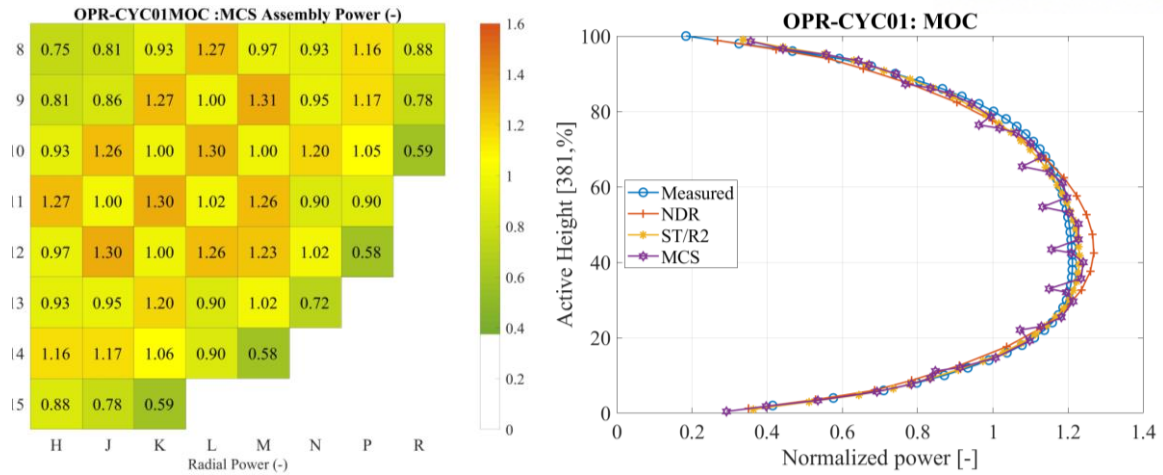
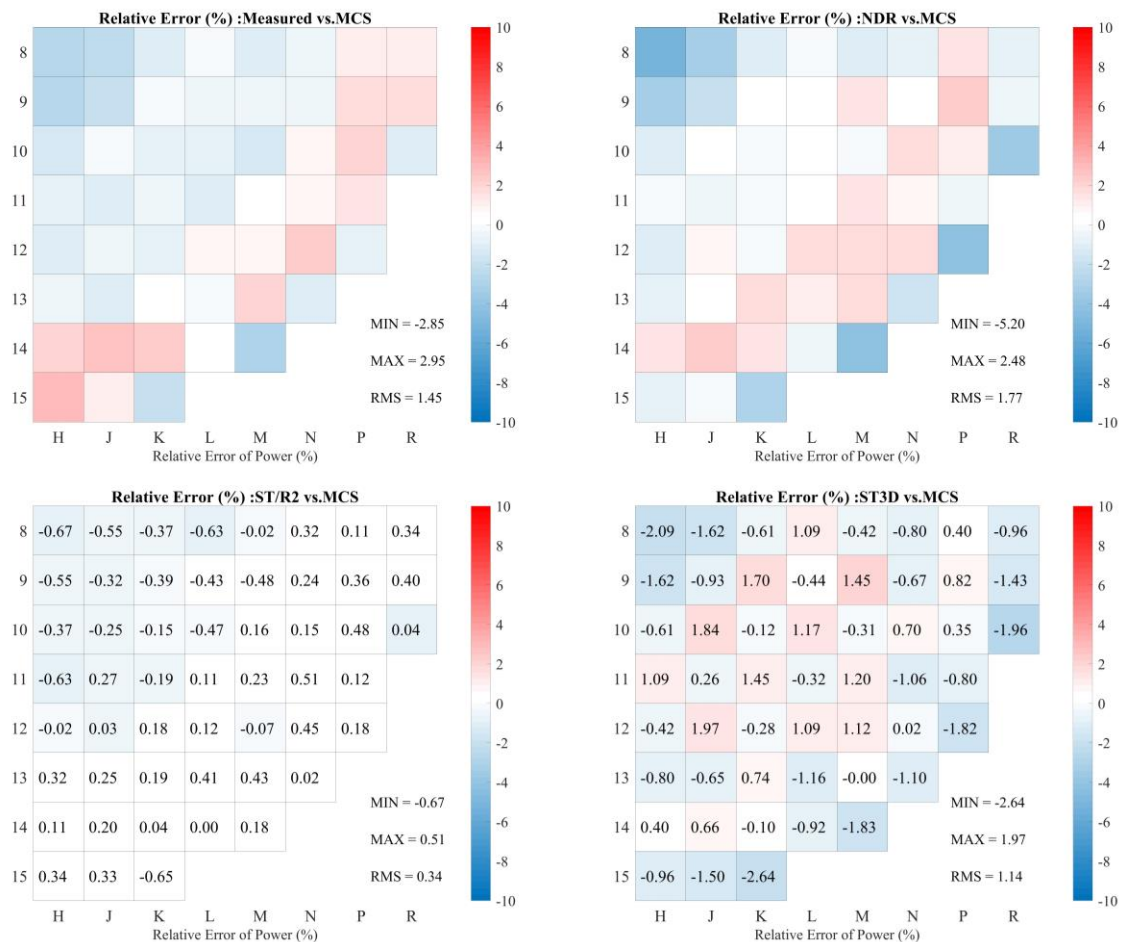


Figure 20. Axial power distribution at BOC Cycle 01.





**Figure 21. MCS radial power distribution and axial power distribution comparison at MOC (6.0 MWD/MT) Cycle 01; NDR = 5 MWD/MT.**



**Figure 22. Relative error of radial assembly power distribution at MOC Cycle 01.**

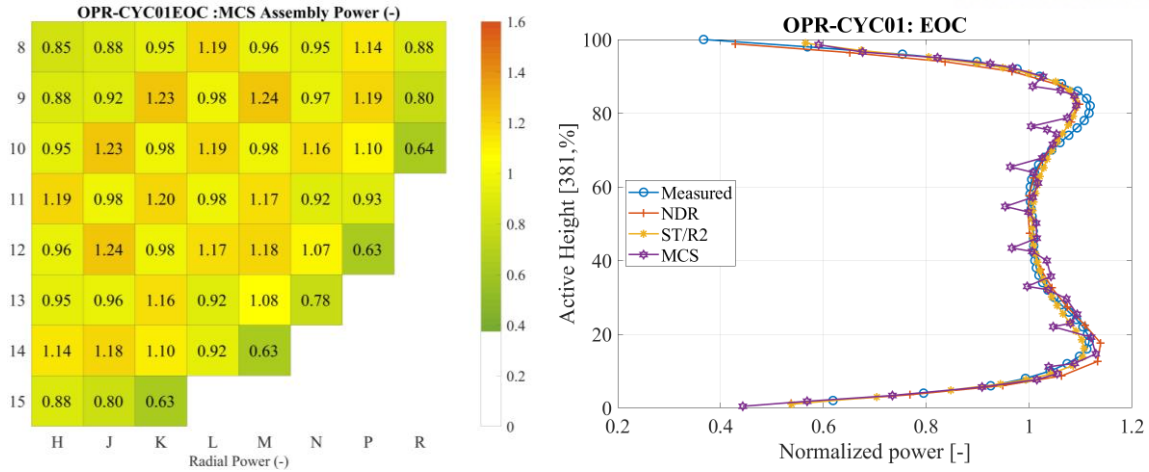


**Figure 23. MCS radial power distribution and axial power distribution comparison at EOC (13.8 GWD/MT) Cycle 01.**

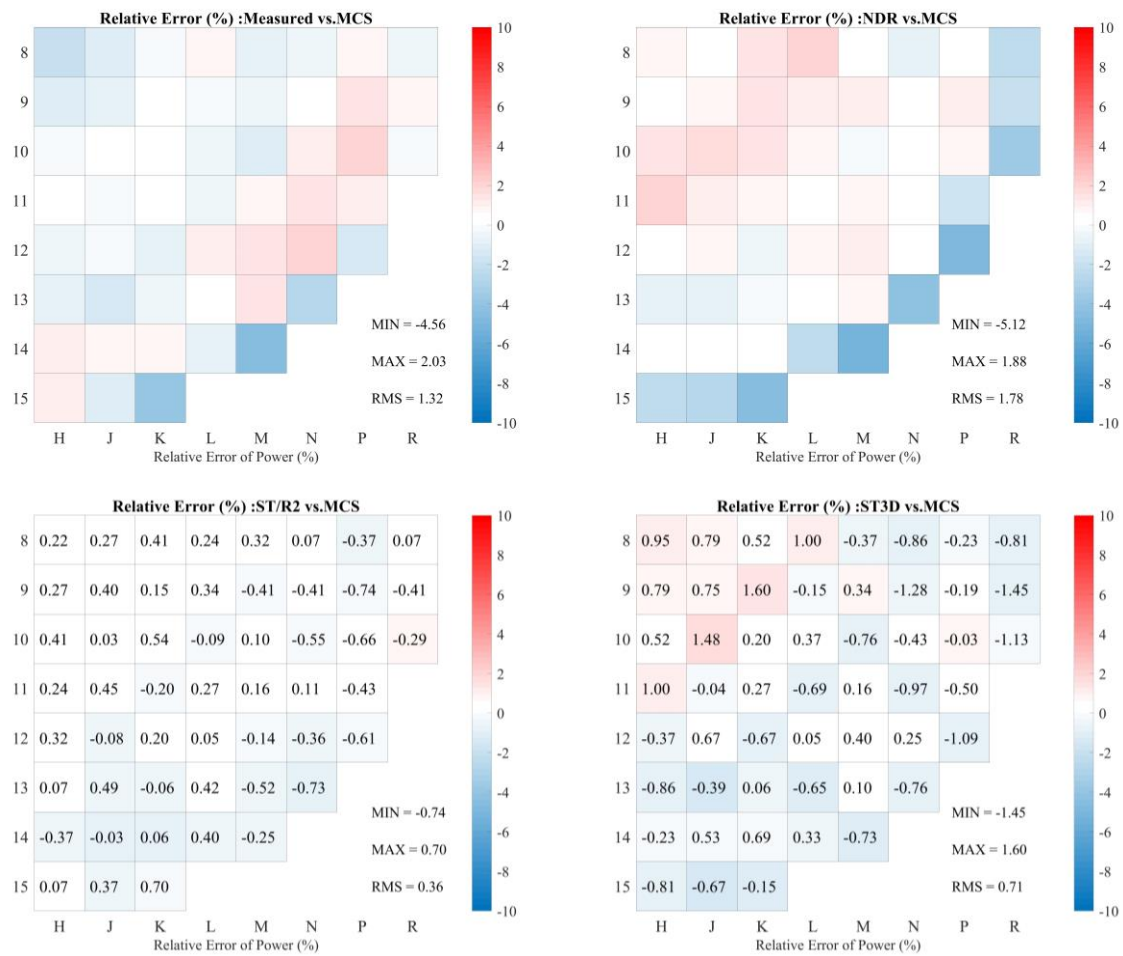


**Figure 24. Relative error of radial assembly power distribution at EOC Cycle 01.**

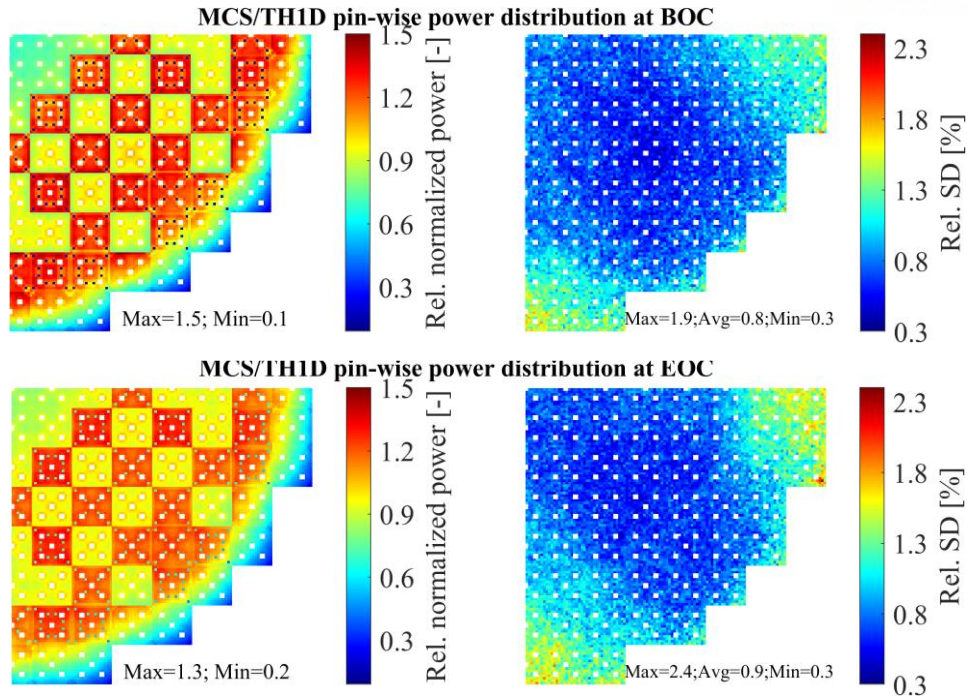


Figure 25. Axially integrated pin-power and uncertainty of MCS/TH1D at BOC and EOC.

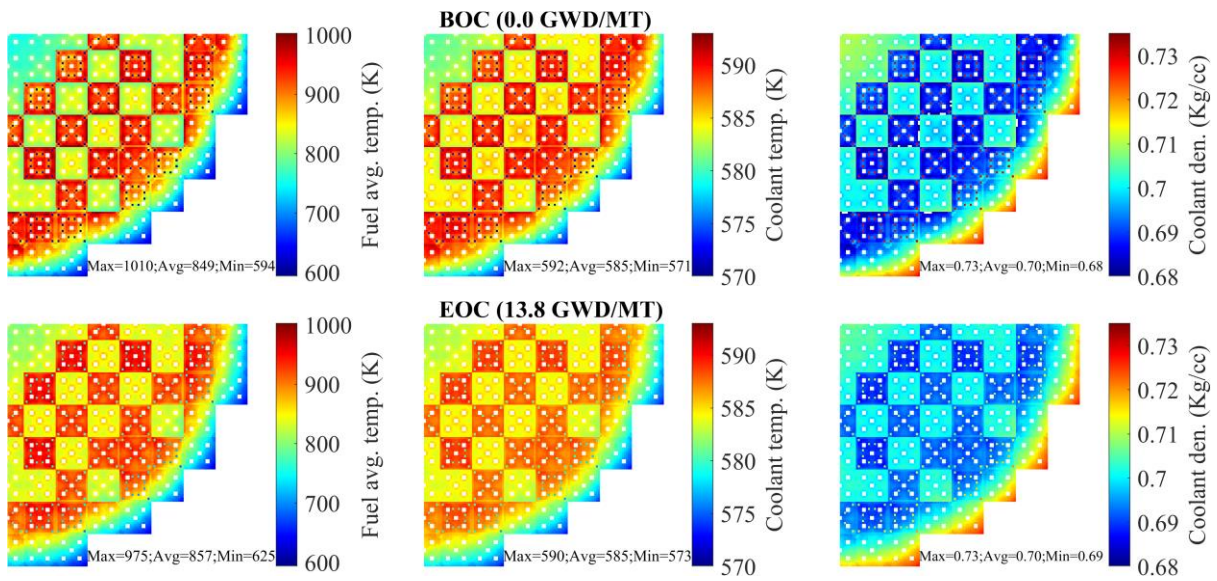
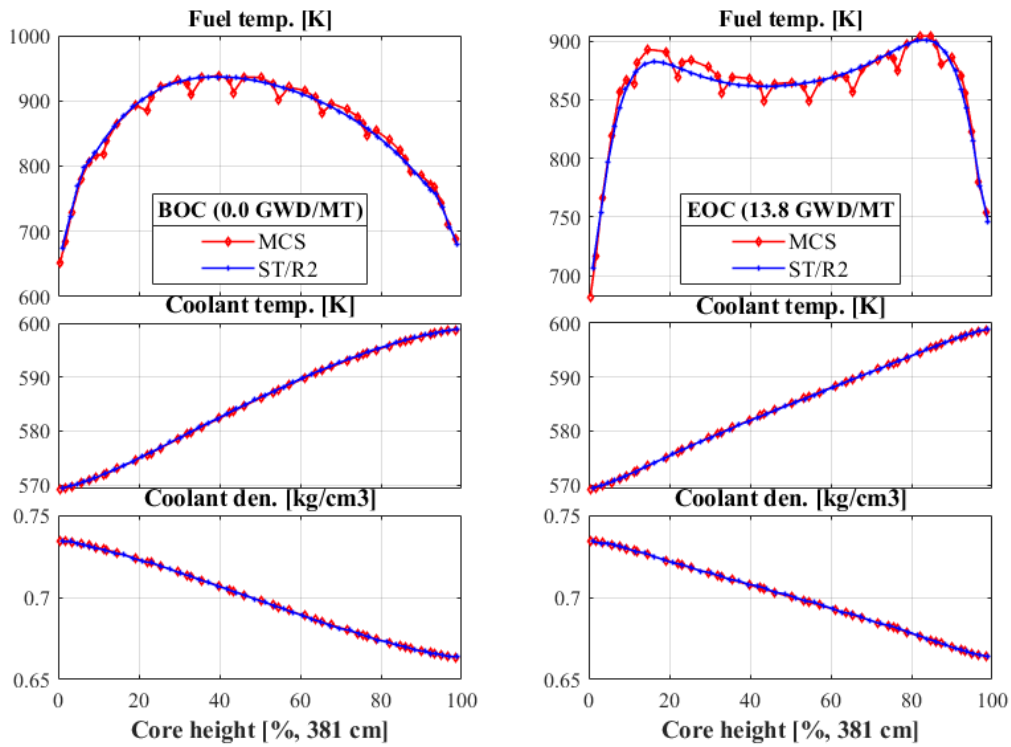


Figure 26. Axially integrated pin-by-pin distribution of MCS/TH1D at BOC and EOC.



**Figure 27. Axial distribution of MCS/TH1D against ST/R2 at BOC (left) and EOC (right).**

#### 4.4.3. MCS multi-physics couplings vs. Measured data

MCS, coupled with TH1D, showed good agreement with measured data and other reference codes. Therefore, the study of MCS/CTF and /FRAPCON will be simulated for the OPR-100 quarter-core system at Cycle 1 with the same conditions (number of particles, number of divisions in axial and radial radiation) as in MCS/TH1D. In this section, the MCS MP coupling results are compared against the experimental data because the verification of MCS/TH1D MP capability and accuracy for the OPR-1000 system had shown good agreement in section 4.4.2 with NDR, ST/R2, and ST3D. However, the results obtained from the reference code will be used if the measured data is not provided.

##### a. Summary of comparison between MCS MP couplings

The summary of the simulation time and memory of the three coupled systems are listed in Table 8. It shows that MCS/CTF required a larger number of simulations compared to MCS/TH1D and MCS/FRAPCON and MCS/TH1D required smaller memory than others. Table 9 provides a summary of fuel and outlet temperature in MCS couplings. Overall, the MCS coupling models provide similar coolant outlet temperatures. The FRAPCON shows the highest maximum fuel temperature value compared to others. Discussion of CBC results in MCS is shown in Table 10 and the relative error of



power distribution results against the measured data are summarized in Table 11. The CBC results at BOC show that MCS coupled with TH or FP solver resulted in a smaller CBC than without the feedback. The CBC result of MCS/FRAPCON has 30 ppm smaller than without the feedback due to the use of an accurate model, including dynamic gap conductance and fuel thermal conductivity calculation at each iteration step. MCS/CTF result has 1 ppm smaller than MCS/TH1D, and around 7 ppm higher than MCS/FRAPCON. In terms of solver simulation time, the TH1D result is smaller than in FRAPCON even they use the same 1D closed channel. And for the sub-channel code, CTF shows extremely long simulation compared to FRAPCON and TH1D. The MCS will generate 52 inputs representing each assembly in the quarter core CTF simulation. There are 72 processors used in these simulations, but only 52 processors were used in the CTF simulation. Due to long simulation time and limitation of having parallel simulation in CTF, the criticality calculation at BOC of MCS/CTF is 3.7 times longer than MCS simulation without the feedback while MCS/TH1D and MCS/FRAPCON are 1.2 and 1.4 times longer than without the feedback, respectively.

**Table 8. Summary of the simulation time and memory in MCS.**

	MCS/TH1D	MCS/CTF	MCS/FRAP
BOC simulation time (core-h) <sup>a</sup>	93	289	106
Total simulation time (core-h)	14,250	21,810	11,977
No. of processor	72	72	96
Memory/ proc. at EOC (GB)	18	20	20
Core-h <sup>a</sup> : simulation time x number of processors			

**Table 9. Summary of calculated fuel and outlet temperature in MCS couplings.**

	BOC			EOC		
	TH1D	CTF	FRAPCON	TH1D	CTF	FRAPCON
Fuel avg. temp. (K)	849.1	849.3	888.7	856.2	854.8	840.6
Fuel max. temp. (K)	1202.2	1205.2	1249.5	1148.3	1138.5	1114.1
Avg. outlet temp. (K)	585.3	585.6	585.1	584.4	584.9	584.6
Max. outlet temp. (K)	598.8	599.2	598.6	598.7	599.2	598.6
Exit temp. (K)	598.9	599.4	598.8	599.0	599.4	598.9

**Table 10. Summary of CBC results and the CBC difference against measured data.**

	MCS/TH1D	MCS/CTF	MCS/FRAPCON
No. of processor	28	84	28
Solver simulation time (s)	0.05	285	61

CBC-BOC (ppm)		732±1	731±1	724±1
<b>CBC errors (Measured-MCS)</b>	3	5	5	2
	4	18	18	14
	5	24	27	20
	6	44	45	39
	7	34	35	31
	8	24	21	18
	9	24	25	20
	10	26	27	20
	11	25	25	21
	12	24	16	19
	13	14	13	12

**Table 11. Summary of relative radial power differences of MCS compared to measured data.**

	BOC* (0.05 MWD/MT)			MOC (6.0 MWD/MT)			EOC (13.8 MWD/MT)		
	Max.	Min.	RMS	Max.	Min.	RMS	Max.	Min.	RMS
MCS/TH1D	2.11	-4.35	1.61	2.95	-2.85	1.45	2.03	-4.56	1.32
MCS/CTF	2.79	-4.41	1.72	3.81	-2.73	1.53	2.07	-3.95	1.26
MCS/FRAPCON	2.64	-5.26	1.78	3.95	-3.02	1.69	2.25	-3.95	1.43
BOC* = Results from NDR used due to unavailability of measured data									
Relative error = 100*(M/MCS -1)									

The changes of CBC as a function of burnup steps and the difference compared to measured data is shown in Figure 28. The MCS results are underestimated compared to measured data by an average of 23 ppm. However, there is almost no significant difference in calculated CBC results between MCS/TH1D and MCS/CTF because the cross-flow has only a slight effect on core reactivity, which is negligible [37, 38] and the maximum different compared to the measured data is around 44 ppm. CBC results obtained from MCS/FRAPCON show a closer trend to measured data than those in MCS/TH1D and MCS/FRPACON with a maximum difference of 39 ppm, as shown in Table 10. The relative error of MCS radial power distribution compared against the reference at BOC, MOC, and EOC is shown in Figure 29-Figure 32. Overall, good agreement of MCS coupling results compared to reference is illustrated with RMS of relative difference less than 1.8%. MCS results are compared to NDR at BOC due to the unavailability of measured data. The NDR data is obtained using the DIT/ROCS two-step methods code with a closed-channel model for the coolant flow similar to TH1D. Therefore, the NDR result is closer to MCS/TH1D than in MCS/CTF and MCS/FRAPCON. MCS MP coupled results show

large discrepancies compared to measured data, especially at the center and the core-periphery where the power uncertainty is relatively high. Figure 32 illustrates the axially-integrated power compared to measured data, and Figure 33 illustrates the axial fuel temperature, coolant temperature, and density parameters compared against the available ST/R2 results. The figure shows a similar trend of the calculated MCS results as in assembly and 2x2 assemblies' core results. The large discrepancies of fuel temperature in FRAPCON are due to dynamic gap conductance and thermal conductivity, as shown in Figure 34 and 35. The gap conductance in FRAPCON is increased as a function of burnup while in TH1D and CTF, it remained constant. The thermal conductivity in FRAPCON is also increased as the burnup increased compared to those in TH1D and CTF. Therefore, the calculated fuel temperature in FRAPCON is lower than those in TH1D and CTF at low burnup; as burnup increase, the calculated fuel temperature in FRAPCON become lower than those in TH1D and CTF.

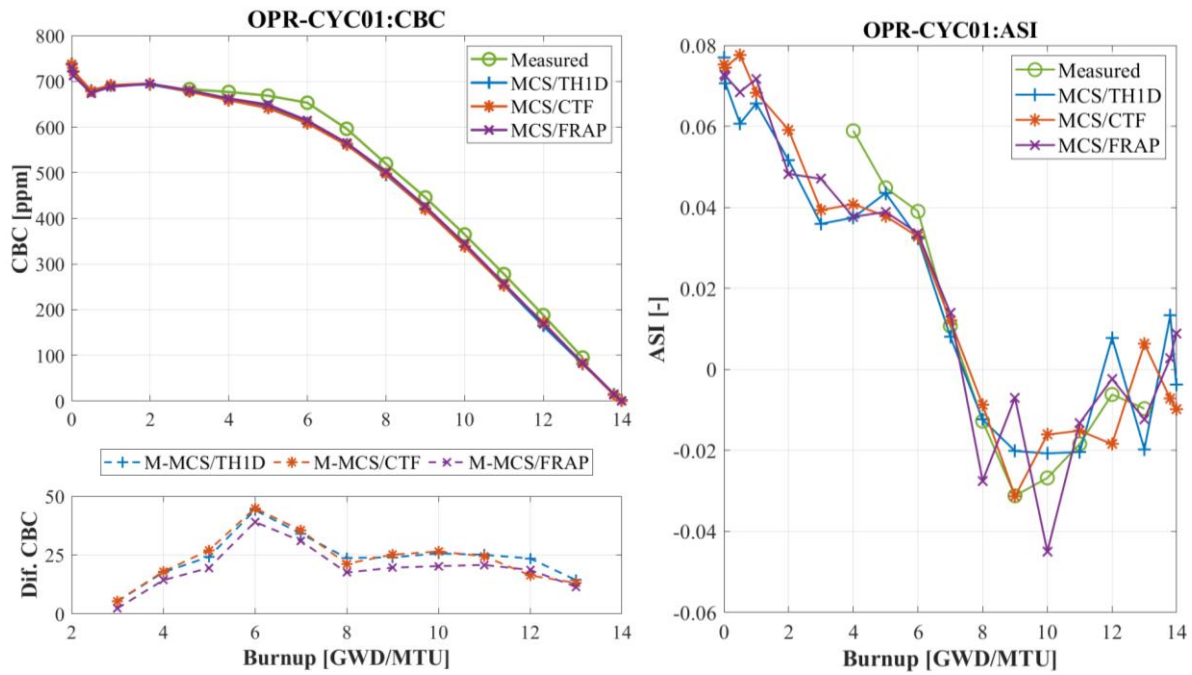


Figure 28. Boron letdown curves and ASI of MCS MP coupling against measured data.

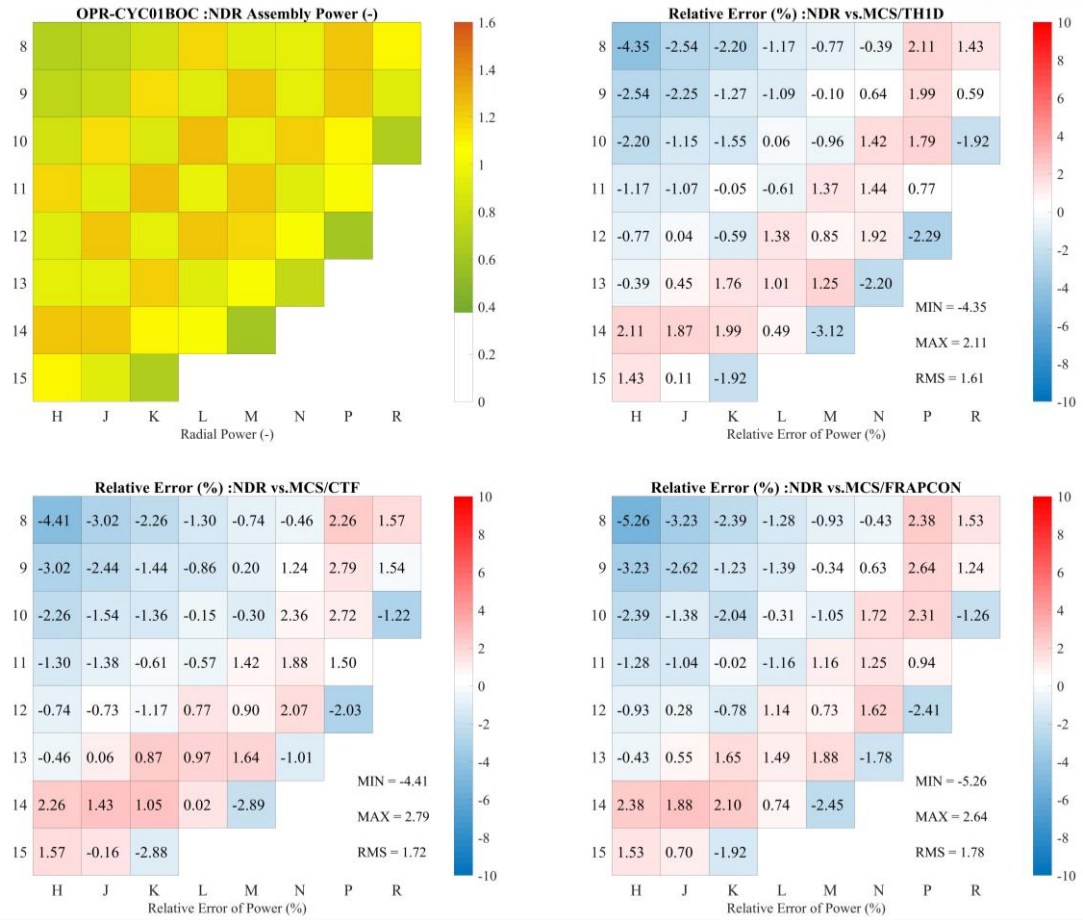
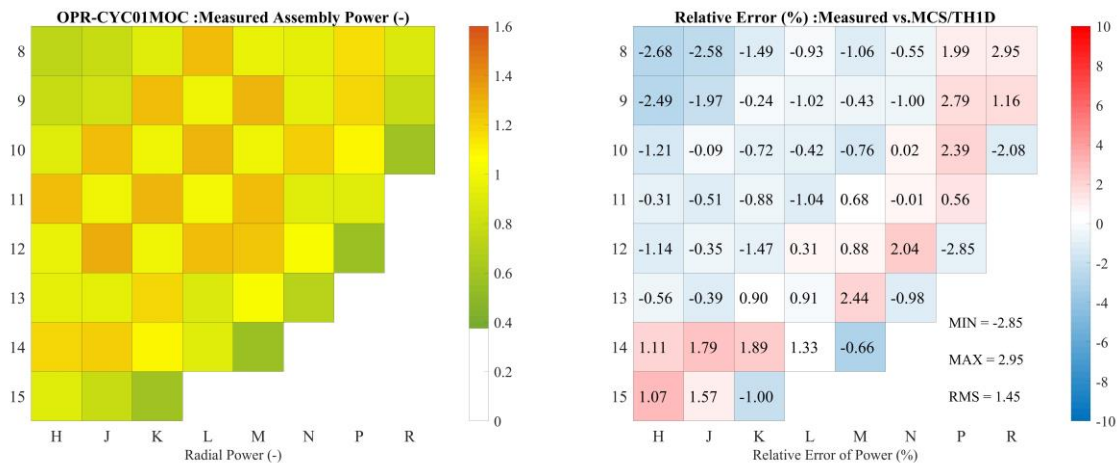
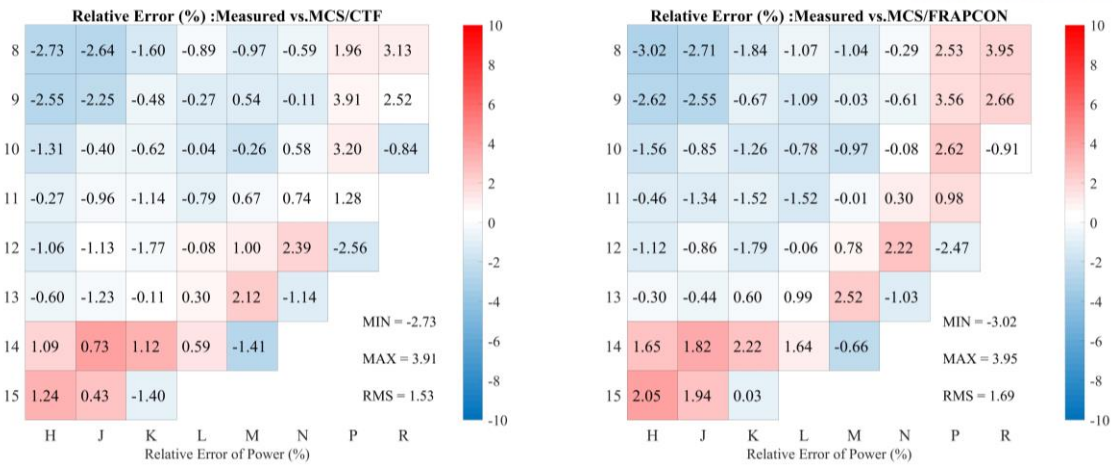


Figure 29. NDR assembly power (top left) and relative error compared to MCS MP coupling results at BOC (0.05 GWD/MT) Cycle 01.







**Figure 30. Measured assembly power and relative error compared to MCS MP couplings at MOC (6.0 GWD/MT) Cycle 01.**

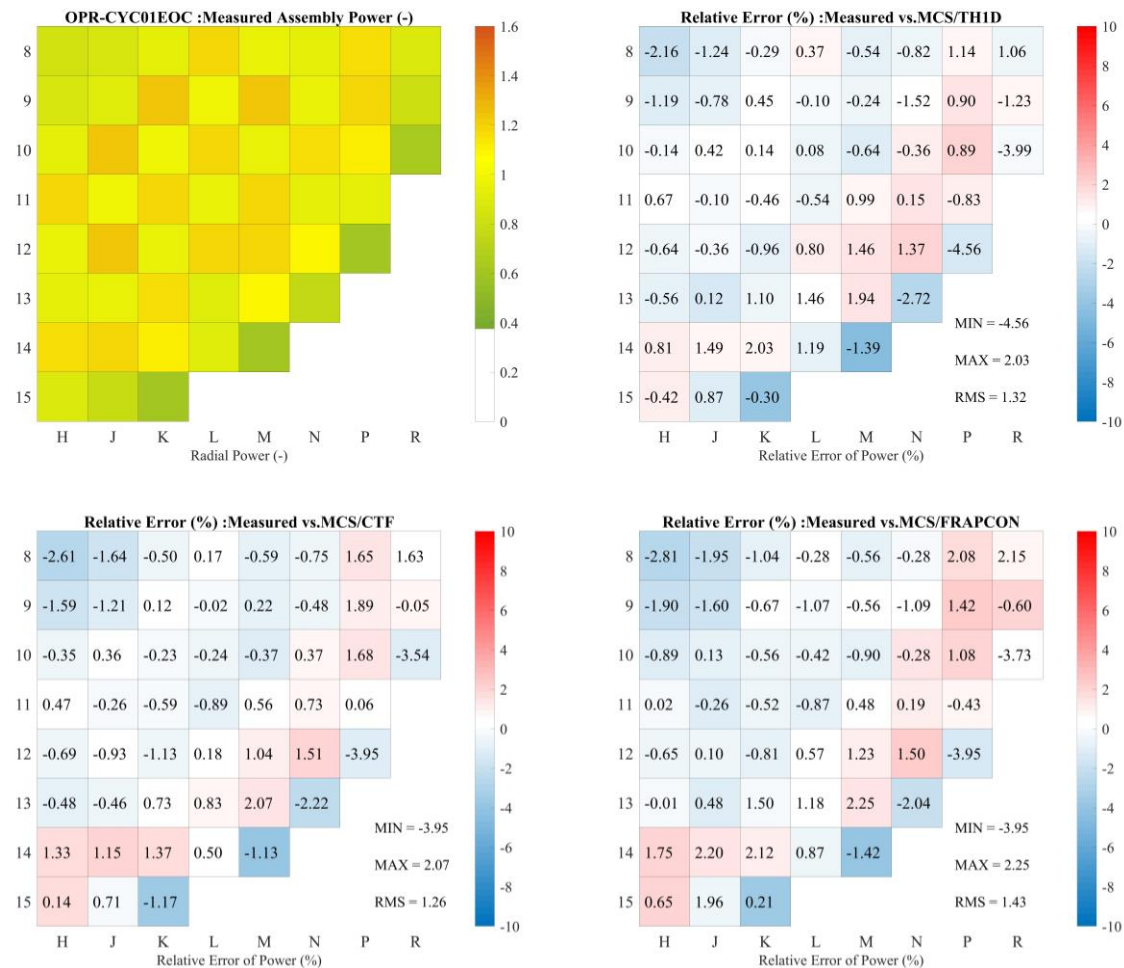


**Figure 31. Measured assembly power and the relative error of MCS MP couplings at EOC (13.8 GWD/MT) Cycle 01.**

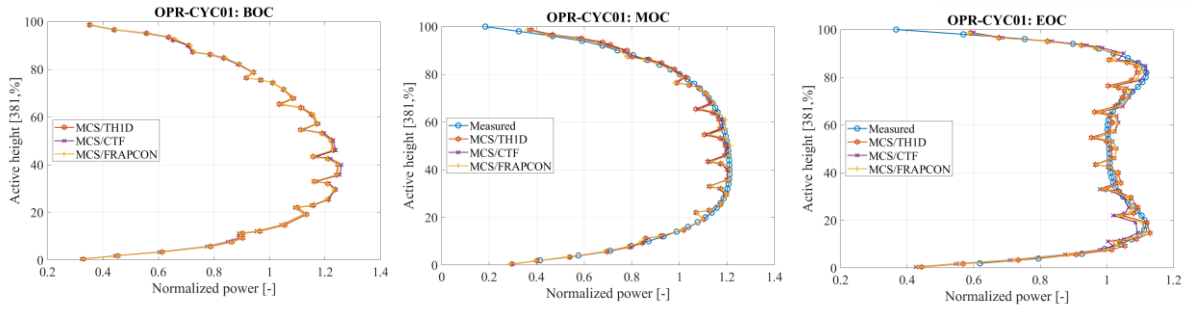


Figure 32. MCS MP couplings results of axial power distribution against the measured data.

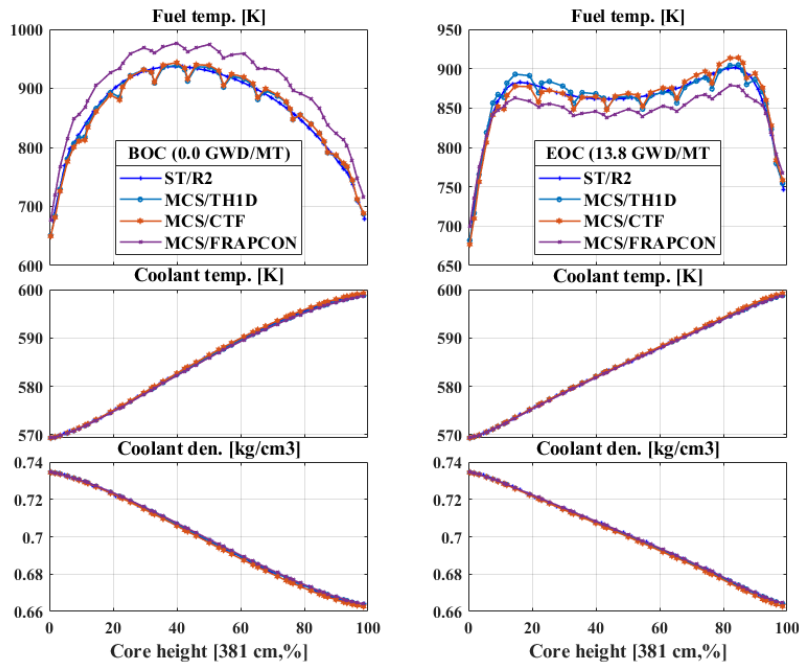


Figure 33. Axial distribution of MCS against ST/R2 at BOC (left) and EOC (right) Cycle 01.

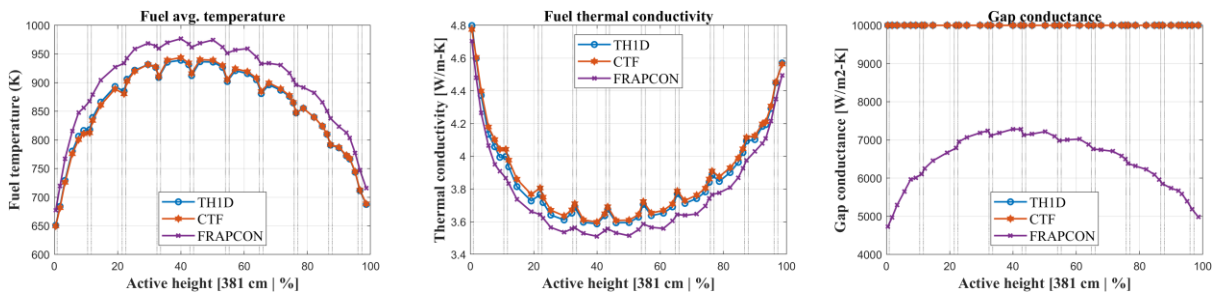
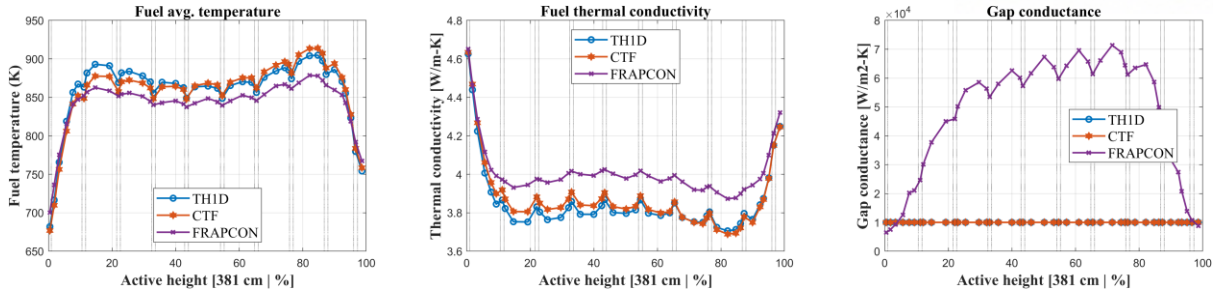


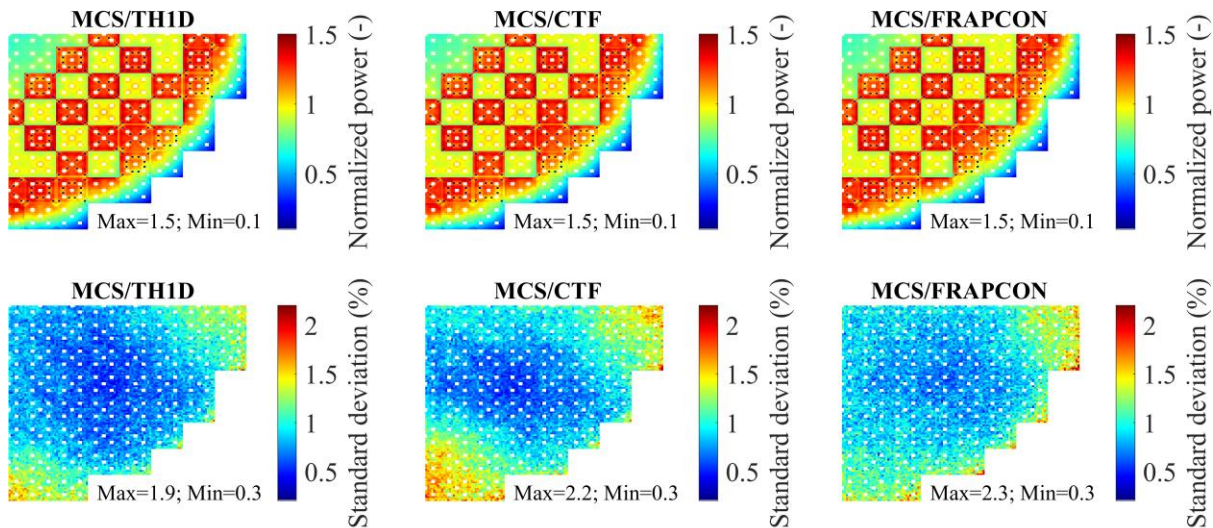
Figure 34. MCS axial fuel temperature, thermal conductivity, and gap conductance comparison at BOC (0.0 GWd/MT).



**Figure 35. MCS axial fuel temperature, thermal conductivity, and gap conductance comparison at EOC (13.8 GWD/MT).**

### b. Pin-wise distribution comparison

The axially-integrated pin-wise distribution results of MCS/TH1D and the relative difference compared to MCS/CTF and MCS/FRAPCON at BOC and EOC are shown in Figure 36-Figure 43. Figure 36 and Figure 37 show that the pin-wise power distribution of three MCS coupling systems becomes smoother as the burnup increases from BOC to EOC. However, the relative power difference of MCS/TH1D compared to MCS/CTF and MCS/FRAPCON also increased as a function of burnup due to the negative feedback from the fuel temperature drop at higher burnup [17]. The maximum value of the relative standard deviation in MCS/TH1D is 1.9% and 2.37% at BOC and EOC, respectively. Considering the relative difference in power distribution of three coupled systems with MCS/TH1D as a reference, it seems like random oscillation is mainly caused by uncertainty in MCS while tallying the power.





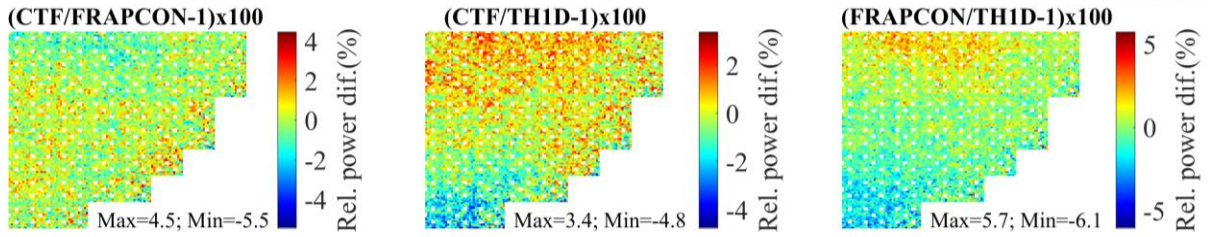


**Figure 36. Power distribution of MCS and relative differences at BOC Cycle 01.**

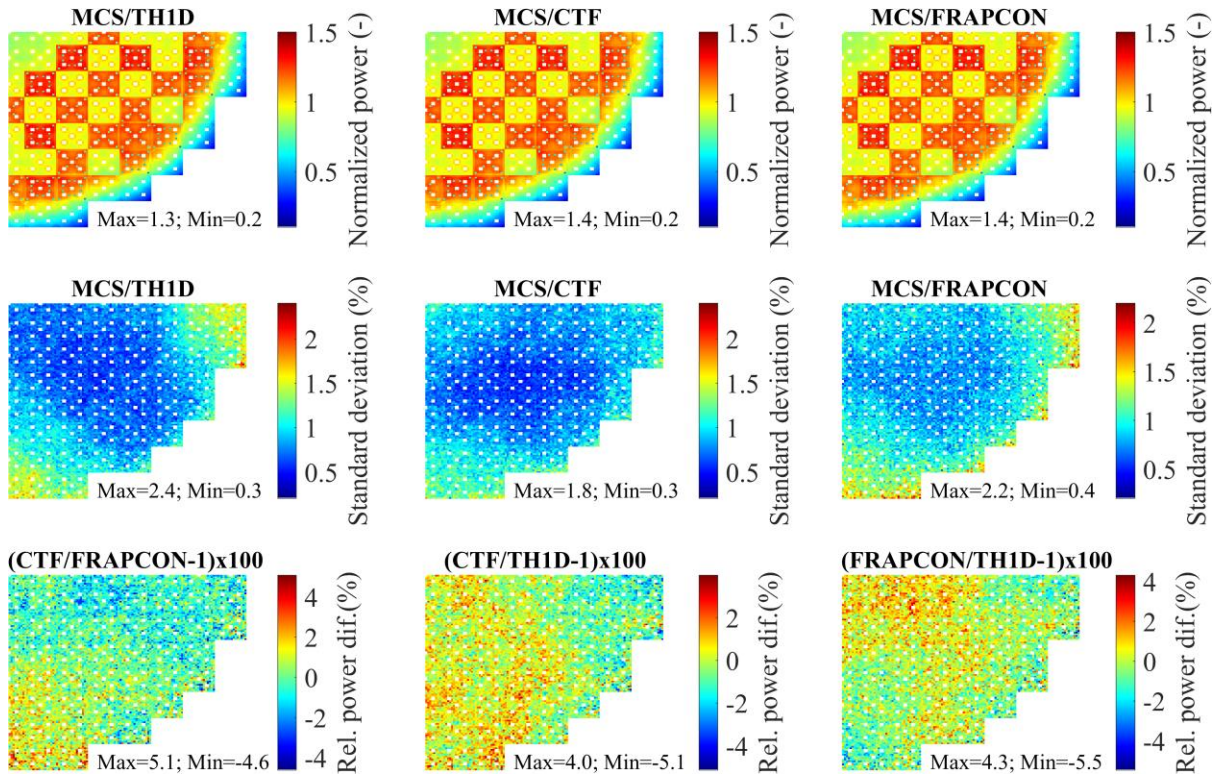


**Figure 37. Power distribution of MCS and relative differences at EOC Cycle 01.**

Figure 38 and Figure 39 illustrate the fuel temperature distribution at BOC and EOC, respectively, with temperature decreasing as a burnup function. The temperature drop from BOC to EOC is approximately 5% in MCS/FRAPCON while the drop is around 3.4% in MCS/CTF, and MCS/TH1D. The fuel temperature distribution comparison of MCS/FRAPCON to MCS/TH1D and MCS/CTF shows large discrepancies with the maximum relative difference at BOC of 6.3% and 6.9%, respectively, for three reasons. First, the large difference occurs at low power assemblies (center) and in the core-periphery where the power is relatively low. Second, it is caused by the different formulas of thermal conductivity models in the fuel pellet in FRAPCON compared to TH1D and CTF. In FRAPCON, the thermal conductivity is calculated as a function of burnup, temperature, and density. However, the thermal conductivity in TH1D is a fuel burnup independent, and the simplified formula is used. Third, FRAPCON applies the dynamic gap-conductance of the fuel-cladding gap, which is dependent on temperature, emissivity, gas composition, gas pressure, surface contact, all of which change with burnup

[39]. The gap is the thermal barrier decreases with increasing burnup and needs to be calculated after every iteration. However, TH1D and CTF employ only a constant gap conductance for the entire calculation. Therefore, FRAPCON is better used in safety analysis because it is more conservative and accurate than TH1D and CTF.

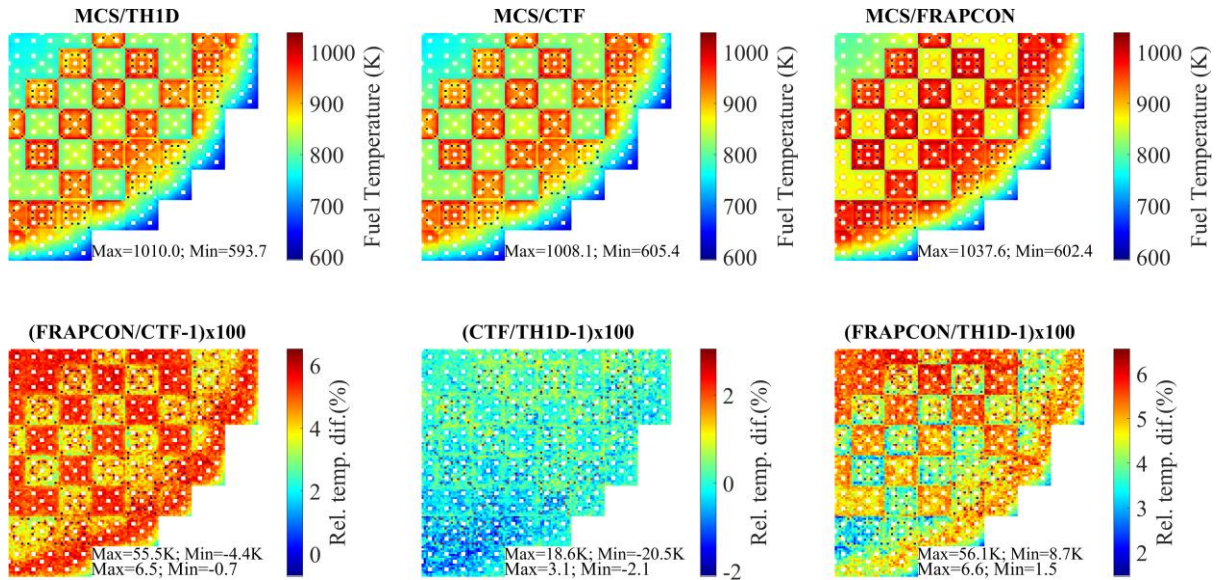


Figure 38. Fuel temperature distribution of MCS and relative differences at BOC Cycle 01.

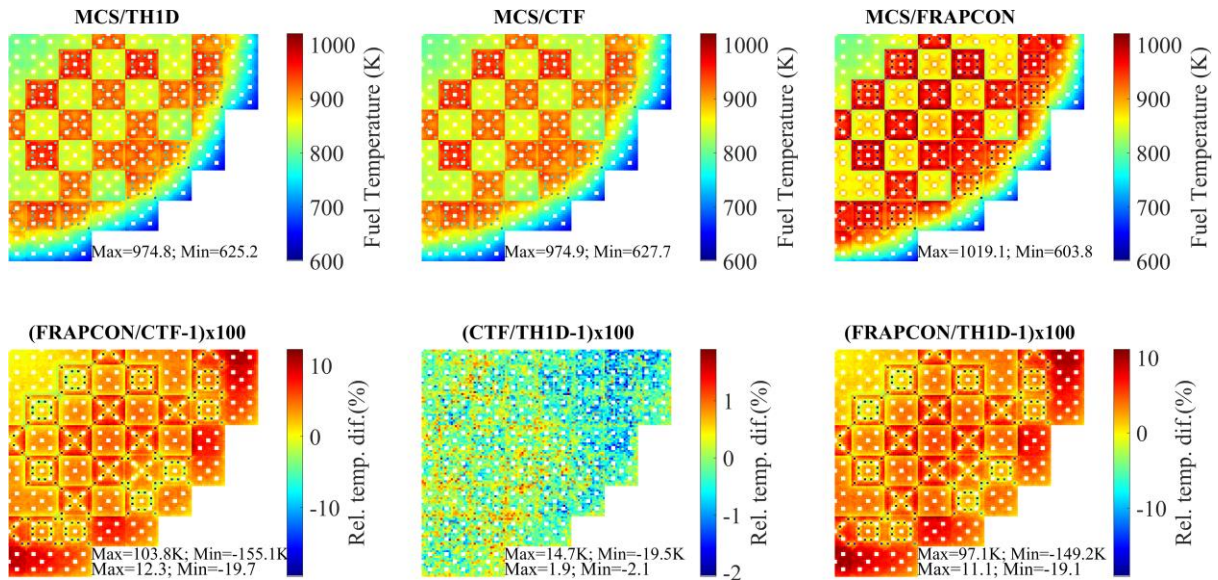


Figure 39. Fuel temperature distribution of MCS and relative differences at EOC Cycle 01.

Figure 40-Figure 43 illustrate the coolant temperature and density distribution and their relative differences. The TH1D uses a 1D enthalpy rise model, and FRAPCON uses the heat capacity to determine the coolant temperature distribution. However, they show no significant differences in coolant temperature and densities with a maximum relative difference of 0.1% and 0.73%, respectively.



The coolant temperature distribution at outlet when using CTF shows no clear border among adjacent assemblies as those assemblies in FRAPCON and TH1D solvers' results. This significant difference again is from the lateral cross-flow in the CTF module while TH1D and FRAPCON solver does not simulate the cross-flow between adjacent assemblies. The cross-flow model in CTF provides more realistic coolant temperature and density distribution (smooth distribution) than FRAPCON and TH1D without the cross-flow.

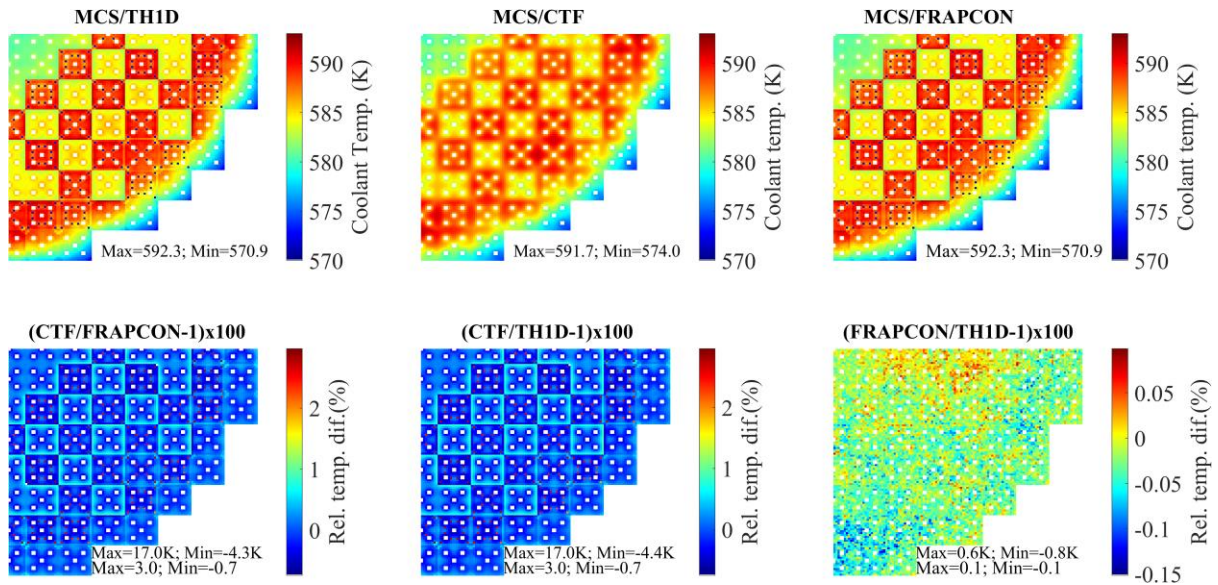


Figure 40. Coolant temperature distribution of MCS and relative differences at BOC Cycle 01.

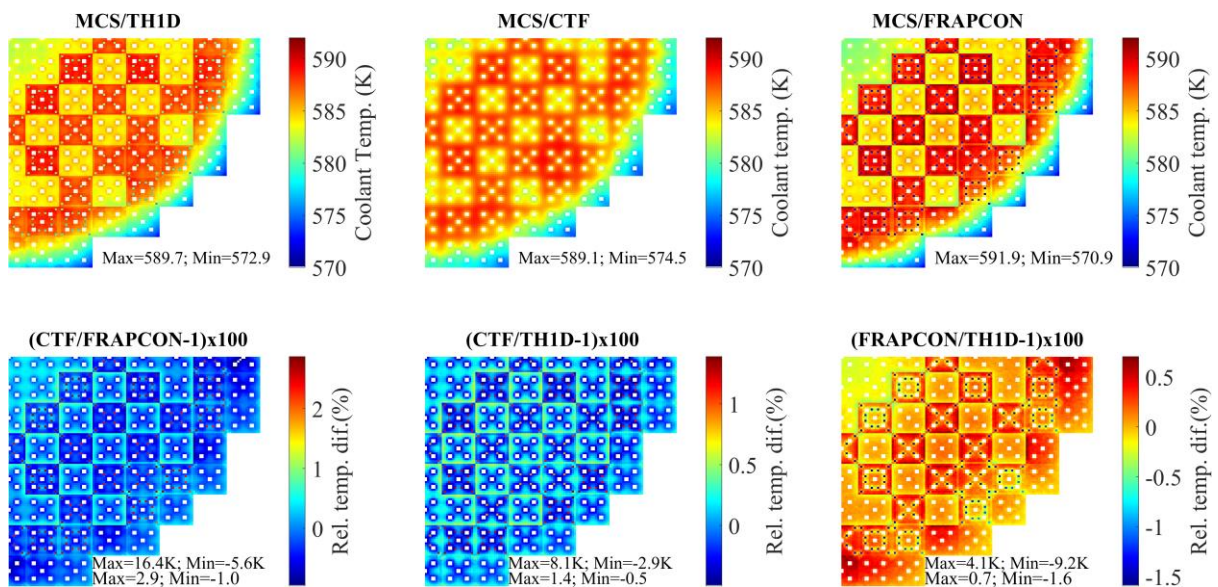


Figure 41. Coolant temperature distribution of MCS and relative differences at EOC Cycle 01.

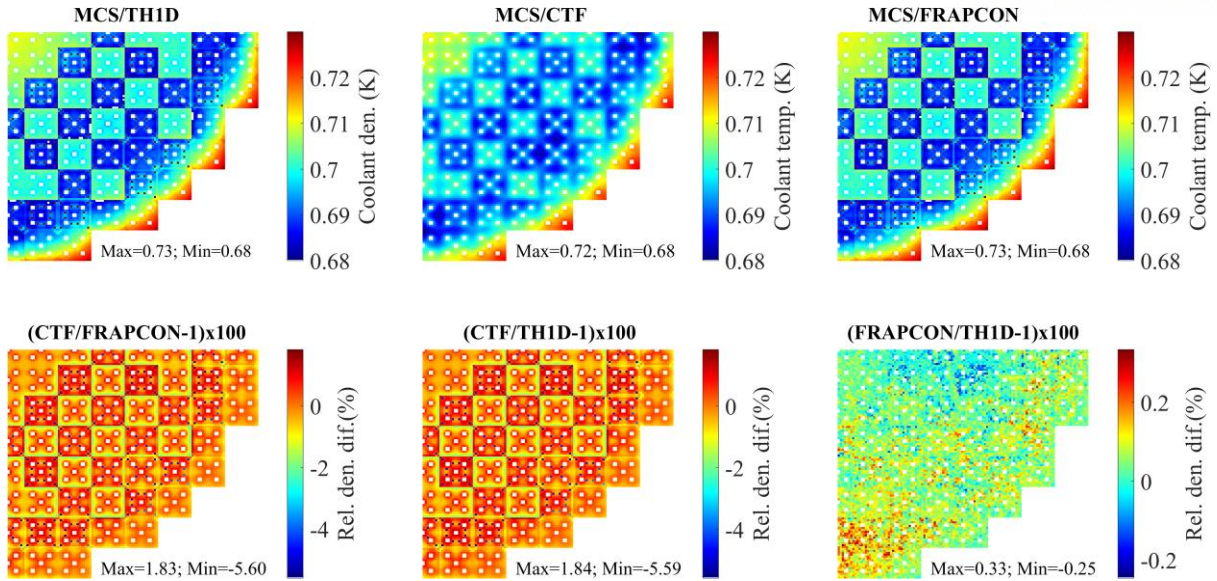


Figure 42. Coolant density distribution of MCS and relative differences at BOC Cycle 01.

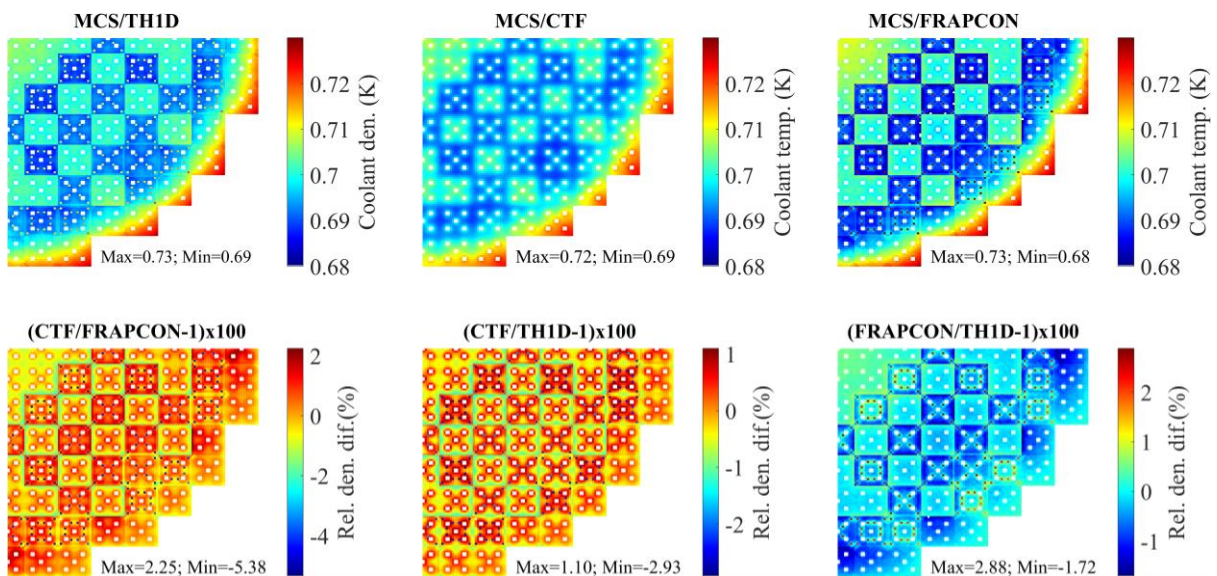


Figure 43. Coolant density distribution of MCS and relative differences at EOC Cycle 01.

#### 4.5. MCS Multi-cycle Simulation Analysis

In each burnup calculation step, MCS outputs the number densities of each burnup cell, CBC, pin, and integrated power profile, temperature profile, and burnup profile, for further analysis and post-processing. Shuffling, rotating, and refueling functions for the fuel assemblies are implemented in MCS to enable multi-cycle simulation using burned fuel from previous cycles and fresh fuel in the current cycle. The simulation of Cycle 2 uses the burned fuel compositions calculated at the end of Cycle 1 with appropriate shuffling and rotations according to the loading patterns in Figure 8 (right). Figure 44 presents the distributions of  $^{235}\text{U}$  density at Cycle 1 EOC (left) and Cycle 2 BOC (right) (the blank



assemblies for Cycle 2 BOC are fresh fuel assemblies which have been removed from the figure for clarity).

The clock wall simulation time for Cycle 2 with 28 burnup steps (totaling 14.453 GWD/MTU GWD/MTU) on 66 CPUs amounts to 237 h wall-clock time (~15,655 core-h) on “2.8 GHz, Intel (R) Xeon (R) CPU”. The MCS multi-cycle results are compared against measured data and result from ST/R2 and NDR in Figure 45-49. Figure 45 displays the boron letdown curves and the differences between MCS results and measured data, NDR data, ST/R2, and ST3D results (notice that no measured data is available at BOC). The calculated CBC of MCS underestimates the measured data with a maximum difference of about 37 ppm ( $1\sigma = 1$  ppm) at 4 GWD/MT. The CBC of MCS is within 22 ppm compared to NDR data, the ST/R2, and ST3D code results. Figure 46-48 illustrate the normalized assembly power distribution on MCS/TH1D and the relative differences compared to the references at BOC, MOC, and EOC. Good agreement is observed between MCS and the references with a maximum RMS error of less than 1.9% throughout all states. Figure 49 shows the normalized axial power profile of MCS/TH1D compared with the references at BOC, MOC, and EOC. Figure 50 presents the axially integrated relative pin-power profile and its relative statistical uncertainty, fuel temperature, coolant temperature, and density of MCS/TH1D results at BOC and EOC. Figure 50 illustrates the pin-wise distribution in MCS at BOC and EOC Cycle 02.

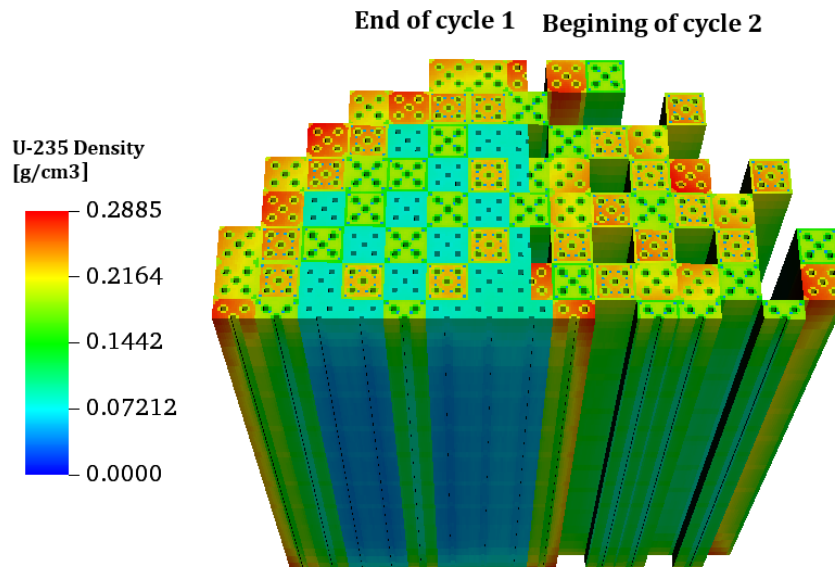


Figure 44. U-235 density at Cycle 01 EOC (left) and Cycle 02 BOC (right).

Table 12. Summary of MCS/TH1D V&V of the relative power differences<sup>a</sup>.

	BOC (0.0 MWD/MT)			MOC (7.0 MWD/MT)			EOC (14.0 MWD/MT)		
	Max.	Min.	RMS	Max.	Min.	RMS	Max.	Min.	RMS



<b>M<sup>b</sup></b>	4.76	-3.12	1.81	3.52	-3.12	1.88	3.35	-5.05	1.68
<b>NDR</b>	3.46	-3.39	1.74	3.41	-2.83	1.08	3.35	-5.05	1.68
<b>ST/R2</b>	2.84	-2.26	1.46	1.74	-1.76	1.05	1.76	-1.33	0.87
<b>ST3D</b>	4.07	-3.53	2.26	3.31	-2.54	1.74	2.77	-2.22	1.51
<sup>a</sup> Measured or NDR or ST/R2 or ST3D – MCS;									
<sup>b</sup> Measured									

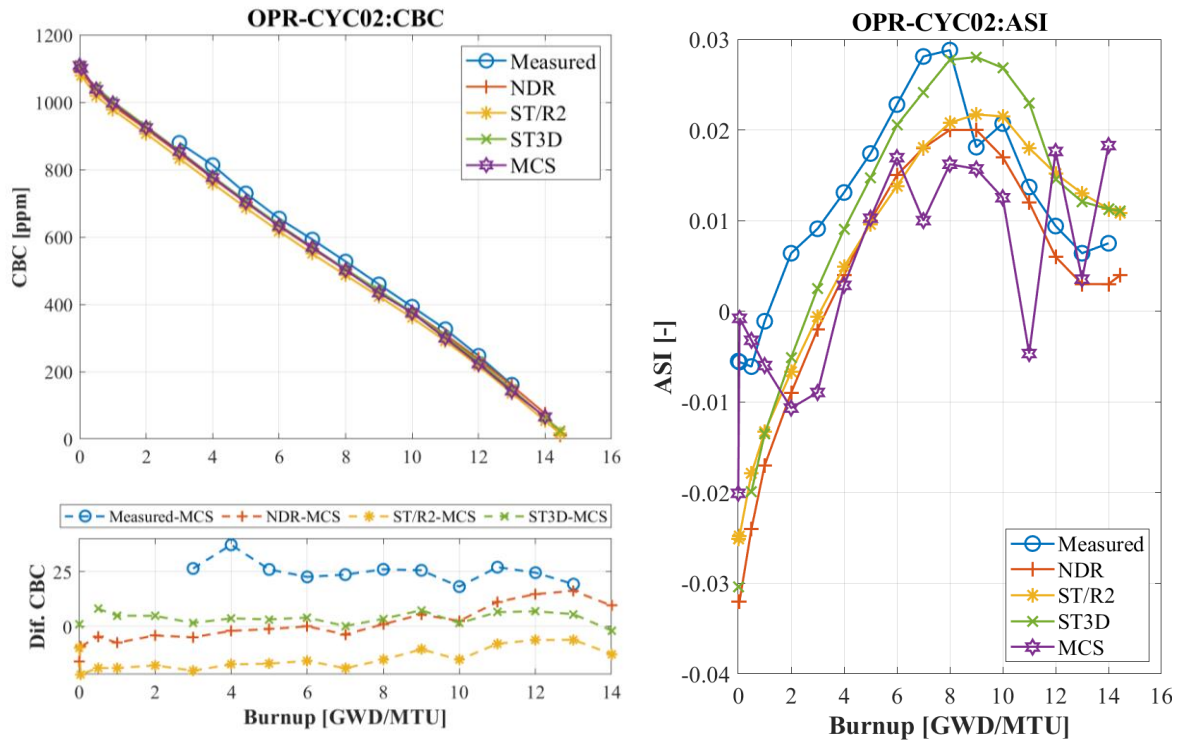
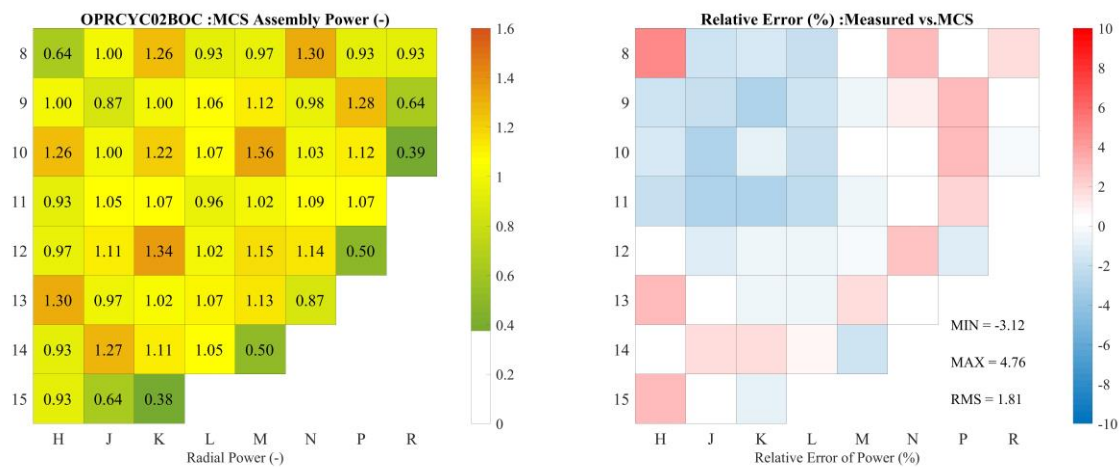


Figure 45. MCS/TH1D V&V of boron letdown and ASI results in Cycle 02.



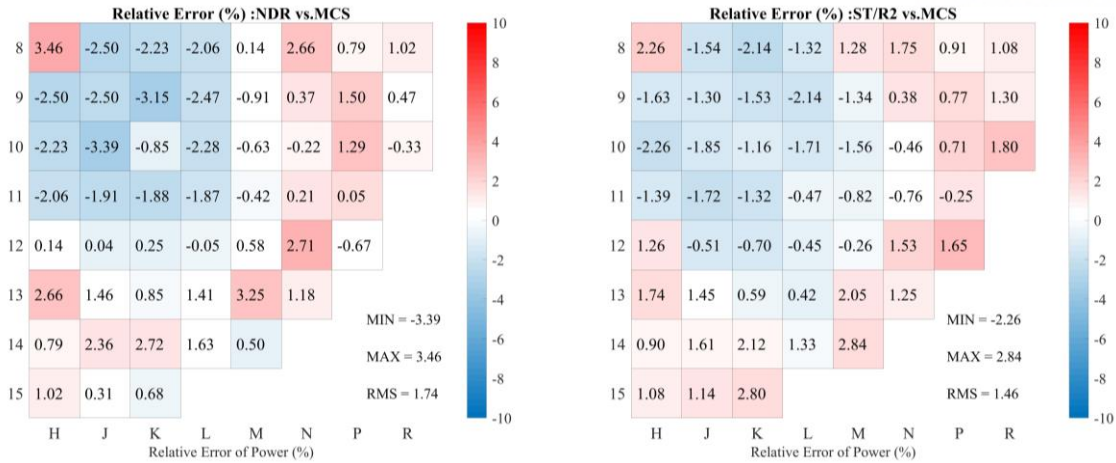


Figure 46. MCS/TH1D radial assembly power and relative error at Cycle 02 BOC.

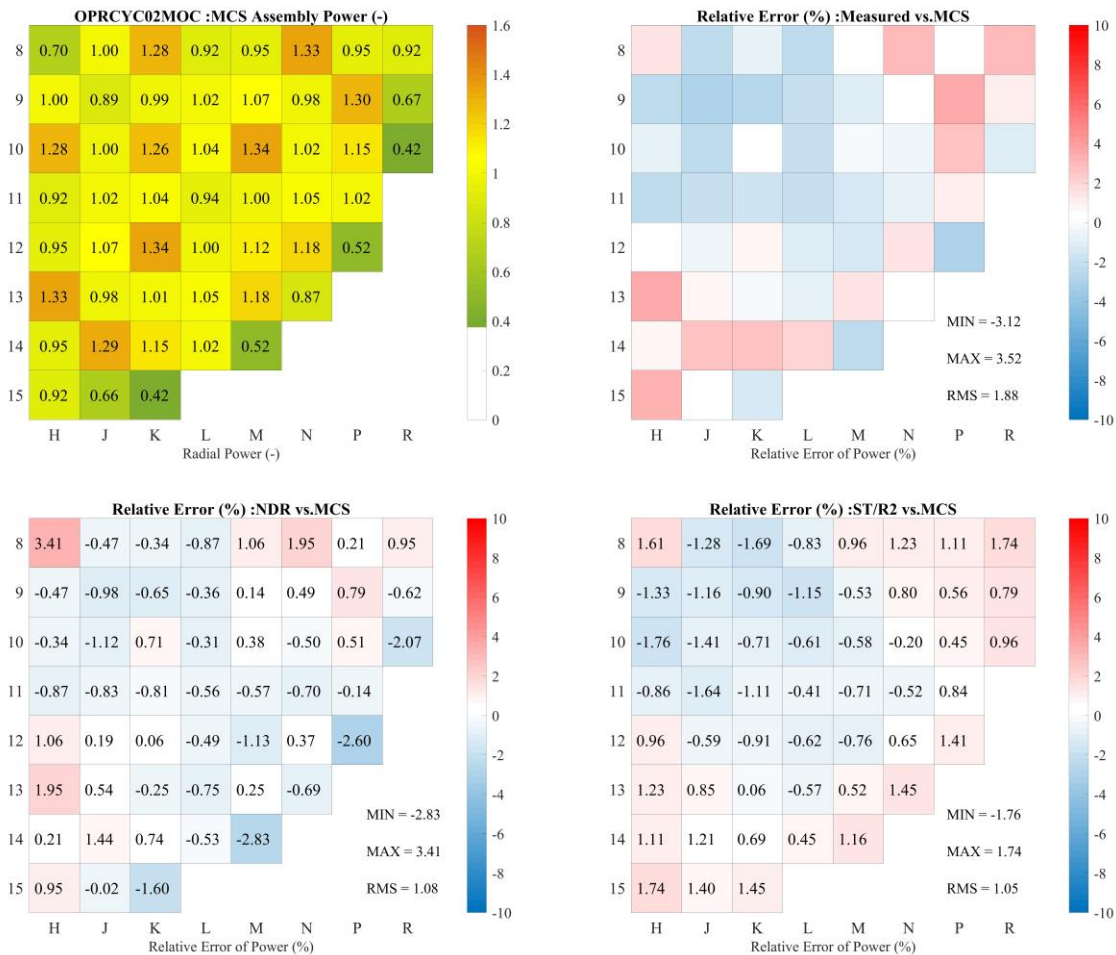


Figure 47. MCS radial assembly power and relative error at Cycle 02 MOC.

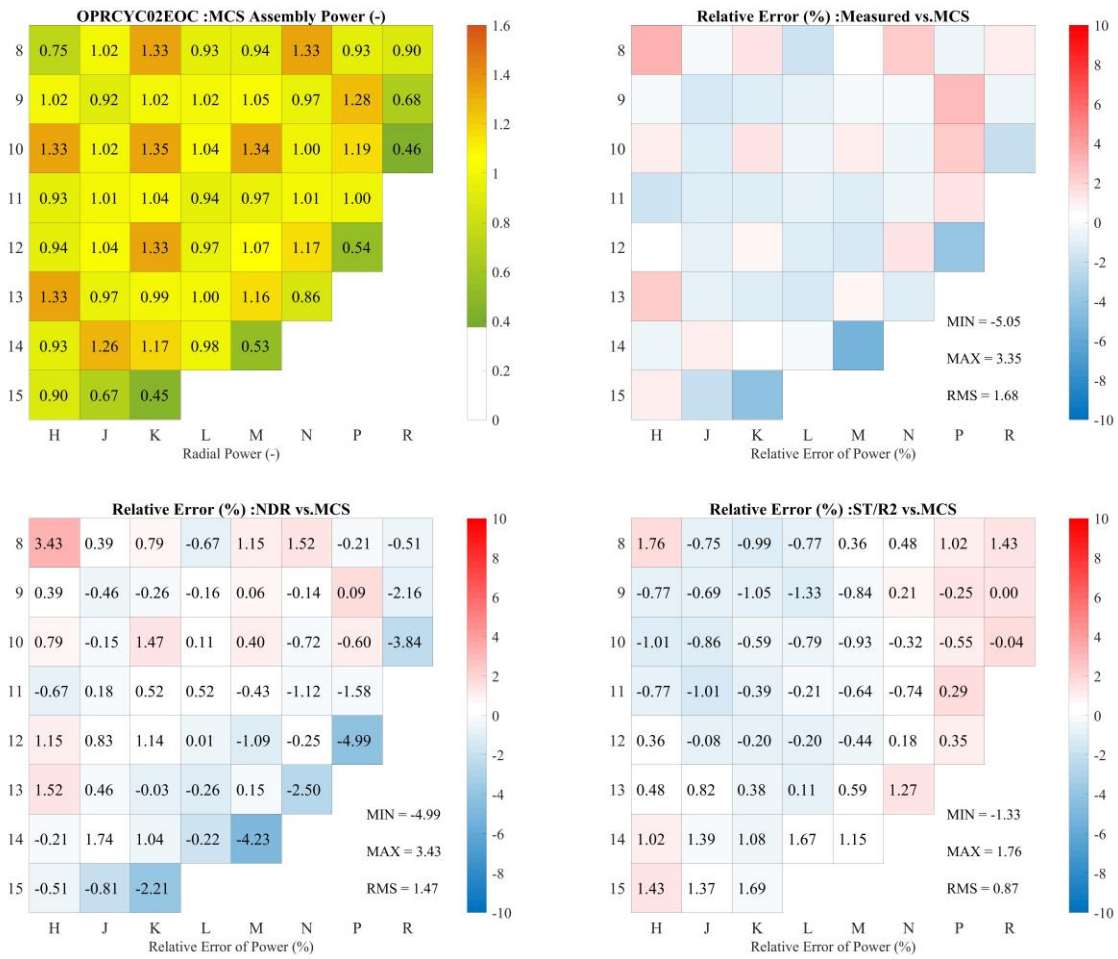


Figure 48. MCS radial assembly power and relative error at Cycle 02 EOC.

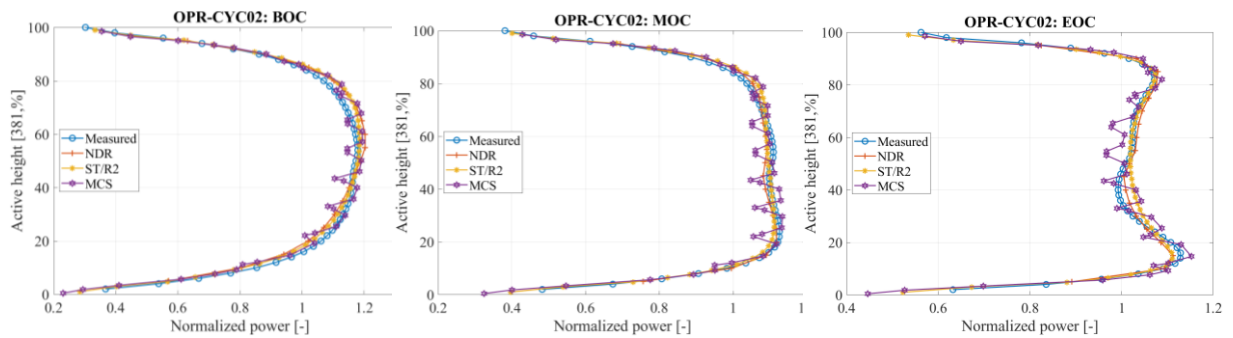
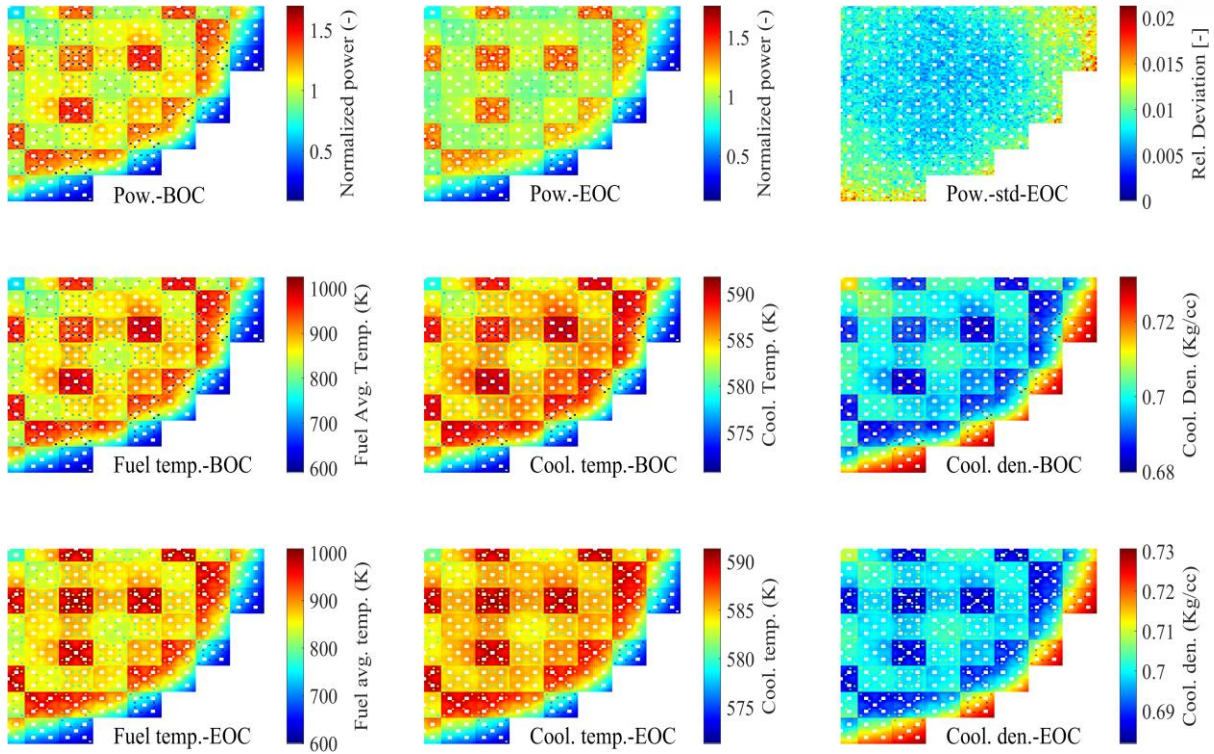


Figure 49. MCS/TH1 axial power distribution Cycle 02.



**Figure 50. Pin-wise distribution at BOC and EOC Cycle 02.**

## V. Conclusion and Perspective

The MCS based MP coupling system of the neutronics along with the 1D closed channel code TH1D, 3D sub-channel TH code CTF, and the steady-state FP code FRAPCON have been developed at UNIST. Overall, these three MCS MP coupled systems improved the neutron transport solution (without the TH feedback), which proved the necessity for coupling the neutronics with the TH or FP to achieve the high-fidelity analysis for the practical large-scale reactor power systems. The verification of the MCS coupled systems was performed on a fuel pin, an assembly, and a 2x2 assembly to check their accuracy and investigate the effects of the three coupled solvers. The highly accurate and efficient MCS based MP coupling code systems were then applied for steady-state, quarter core simulation of a practical OPR-1000 reactor at HFP condition with two consecutive cycles. Overall, the validation and verification study revealed a good agreement between the MCS results and the measurements, as well as the results of other codes. MCS MP coupling results are commonly concordant with the measured data, with CBC error of less than 47 ppm and RMS error of assembly power distribution less than 1.8% in Cycle 1. The restart calculation by refueling, shuffling, and rotation for Cycle 2 with MCS/TH1D simulation also showed good agreement with the measured data, with similar CBC and power distribution errors as Cycle 1. MCS was also compared to the nuclear design report, two-step method code ST/R2, and 3D MOC code STREAM for verification. The three code systems have been demonstrated for high-fidelity MP analyses, and the comparison of power, fuel temperature, coolant



temperature, and density in fuel assembly and pin-level provides a new understanding of the consequence of each code. Among the three MCS MP coupling solvers, MCS/FRAPCON provides a more physical solution than MCS/TH1D and MCS/CTF because FRAPCON has significant advantages over TH codes for predicting the fuel temperature by considering fuel behavior and property changes due to burnup such as thermal conductivity, gap conductance, and other thermal-mechanical parameters. MCS/CTF provides more realistic coolant temperature and density compared to MCS/TH1D and MCS/FRAPCON due to the modeling of cross-flow. In conclusion, it is successfully demonstrated that MCS is capable of coupling with various TH and FP codes for a high-fidelity whole-core analysis in predicting the CBC, power, temperature distribution, and corresponding multi-cycle parameters.

For future work, a convergence study should be performed with CTF to determine the optimum code option for coupled calculation and save simulation time. Another study could explore the complete MP system based on MCS/CTF/FRAPCON coupling since it can provide high fidelity benefitting from the transverse cross-flow between neighboring sub-channels in CTF, and the burnup-dependent fuel thermal conductivity formulation, and iteratively determined fuel pellet-cladding gap thermal conductance in FRAPCON. In addition, the MCS/CTF/FRAPCON coupling system is expected to overcome the drawbacks of the MCS/CTF, such as approximating thermal conductivity and gap conductance and MCS/FRAPCON such as the use of a 1D single-channel model.

## REFERENCES

- [1] S.K. Uzun, Coupled Thermal Hydraulics / Neutronics Analysis of Nuclear Reactors, Thesis (Master), Hacettepe University, 2008.
- [2] T. Viitanen, Serpent-ENIGMA - Combining Monte Carlo Reactor Physics with Fuel Performance, Research report VTT-R-06265111(22).
- [3] D.J. Kelly III, A.E. Kelly, B.N. Aviles, et al., MC21/CTF and VERA multiphysics solutions to VERA core physics benchmark progression problems 6 and 7, Nucl. Eng. Tech. 49 (2017) 1326–1338. <https://doi.org/10.1016/j.net.2017.07.016>.
- [4] K. Wang, Z. Li, D. She, J. Liang, et al., RMC - A Monte Carlo code for reactor core analysis, Ann. Nucl. Energy. 82 (2015) 121–129. <https://doi.org/10.1016/j.anucene.2014.08.048>.
- [5] P.K. Romano, N.E. Horelik, B.R. Herman, et al., OpenMC: A state-of-the-art Monte Carlo code for research and development, Ann. Nucl. Energy. 82 (2015) 90–97. <https://doi.org/10.1016/j.anucene.2014.07.048>.
- [6] J. Leppänen, M. Pusa, T. Viitanen, et al., The Serpent Monte Carlo code: Status, development and applications in 2013, Ann. Nucl. Energy. 82 (2015) 142–150. <https://doi.org/10.1016/j.anucene.2014.08.024>.
- [7] J. Guo, S. Liu, X. Shang, et al., Coupled neutronics/thermal-hydraulics analysis of a full PWR

- core using RMC and CTF, *Ann. Nucl. Energy.* 109 (2017) 327–336.  
<https://doi.org/10.1016/j.anucene.2017.05.041>.
- [8] B.W. Siebert, R.K. Salko, B.N. Aviles, et al., MC21/COBRA-IE and VERA-CS multiphysics solutions to VERA core physics benchmark problem #6, *Progr. Nucl. Energy.* 101 (2017) 338–351. <https://doi.org/10.1016/j.pnucene.2017.05.017>.
- [9] Leppänen. and T. Viitanen, Multi-physics Coupling Scheme in the Serpent 2 Monte Carlo Code, in: *Transactions of American Nuclear Society.* 107 (2012) 1165–1168.
- [10] M. Daeubler, J. Jimenez, V. Sanchez, Development of a High-Fidelity Monte Carlo Thermal-Hydraulics Coupled Code System Serpent / Subchanflow – First Results, in: *Proceedings of the PHYSOR 2014 conference, the Westin Miyako, Kyoto, Japan, Sep. 28–Oct. 3 (2014) 1–16.* <https://doi.org/10.13140/2.1.2400.0326>.
- [11] V. Valtavirta, J. Leppänen, Coupled Burnup Calculations with the Serpent 2 Monte Carlo Code, in: *Proceeding of M&C 2017 conference, Jeju, Korea, Apr. 16–20 (2017).*
- [12] H. Lee, W. Kim, P. Zhang, et al., MCS – A Monte Carlo particle transport code for large-scale power reactor analysis, *Ann. Nucl. Energy.* 139 (2020) 107276.  
<https://doi.org/10.1016/j.anucene.2019.107276>.
- [13] J. Yu, H. Lee, H. Kim, et al., Coupling of FRAPCON for fuel performance analysis in the Monte Carlo code MCS, *Comput. Phys. Commun.* 251 (2020) 106748.  
<https://doi.org/10.1016/j.cpc.2019.03.001>.
- [14] J. Yu, H. Lee, H. Kim, et al., Simulations of BEAVRS benchmark cycle 2 depletion with MCS/CTF coupling system, *Nucl. Eng. Tech.* 52 (2020) 661–673.  
<https://doi.org/10.1016/j.net.2019.09.007>.
- [15] J. Yu, H. Lee, M. Lemaire, et al., MCS based neutronics/thermal-hydraulics/fuel-performance coupling with CTF and FRAPCON, *Comput. Phys. Commun.* 238 (2019) 1–18.  
<https://doi.org/10.1016/j.cpc.2019.01.001>.
- [16] J. Yu, H. Lee, H. Kim, et al., Preliminary coupling of the Thermal/Hydraulic solvers in the Monte Carlo code MCS for practical LWR analysis, *Ann. Nucl. Energy.* 118 (2018) 317–335.  
<https://doi.org/10.1016/j.anucene.2018.03.043>.
- [17] J. Yu, H. Lee, M. Lemaire, et al., Fuel performance analysis of BEAVRS benchmark Cycle 1 depletion with MCS/FRAPCON coupled system, *Ann. Nucl. Energy.* 138 (2020) 107192.  
<https://doi.org/10.1016/j.anucene.2019.107192>.
- [18] J. Yu, S. Lee, D. Lee, Fuel Performance Coupling of FRAPCON within MCS, in: *Transactions of the American Nuclear Society.* 1 (2017) 1416–1419.
- [19] T.D.C. Nguyen, H. Lee, S. Choi, et al., MCS/TH1D analysis of VERA whole-core multi-cycle depletion problems, *Ann. Nucl. Energy.* 139 (2020) 107271.  
<https://doi.org/10.1016/j.anucene.2019.107271>.

- [20] H. Lee, C. Kong, D. Lee, Status of Monte Carlo Code Development At Unist, in: Proceedings of the PHYSOR 2014 conference, the Westin Miyako, Kyoto, Japan, Sep. 28–Oct. 3 (2014).
- [21] B. Ebiwonjumi, H. Lee, P. Zhang, et al., MCS / FRAPCON Multi-physics Coupled Simulation of Westinghouse 3-loop PWR Wholecore Analysis, in: Proceedings of ICAPP conference, Juan-Les-Pins, France, May 12–15(2019). [USB]
- [22] V. Dos, H. Lee, J. Choe, et al., Verification & Validation of MCS Multi-Physics Analysis Capability for OPR-1000 Multi-Cycle Operation, in: Proceedings of M&C 2019 conference, Aug. 25–29 (2019). [USB]
- [23] H. Lee, E. Jeong, H. Lee, et al., Verification of MCS VHTR Modeling Capability, in: Proceedings of RPHA 2017, Chengdu, Sichuan, China, August 24–25 (2017).[USB]
- [24] V. Dos, H. Lee, Y. Jo, et al., Overcoming the challenges of Monte Carlo depletion: Application to a material-testing reactor with the MCS code, Nucl. Eng. Tech. (2020). <https://doi.org/10.1016/j.net.2020.02.003>.
- [25] J. Jang, W. Kim, S. Jeong, et al., Validation of UNIST Monte Carlo code MCS for criticality safety analysis of PWR spent fuel pool and storage cask, Ann. Nucl. Energy. 114 (2018) 495–509. <https://doi.org/10.1016/j.anucene.2017.12.054>.
- [26] T.D.C. Nguyen, J. Choe, B. Ebiwonjumi, et al., Core design of long-cycle small modular lead-cooled fast reactor, Int. J. Energy Res. 43 (2019) 254–273. <https://doi.org/10.1002/er.4258>.
- [27] N.N.T. Mai, P. Zhang, M. Lemaire, et al., Extension of Monte Carlo code MCS to spent fuel cask shielding analysis, Int. J. Energy Res. (2020) 1–14. <https://doi.org/10.1002/er.5023>.
- [28] T.Q. Tuan, J. Choe, X. Du, et al., Neutronic Simulation of China Experimental Fast Reactor Start-up Test- Part II: MCS Monte Carlo Code Calculation, Ann. Nucl. Energy, Accepted for publication (2020).
- [29] H. Lee, Development of a New Monte Carlo Code for High-Fidelity Power Reactor Analysis, Thesis (Doctoral), Ulsan National Institute of Science and Technology, 2019.[USB]
- [30] M. Ryu, Y.S. Jung, H.H. Cho, et al., Solution of the BEAVRS benchmark using the nTRACER direct whole core calculation code, J. Nucl. Sci. Technol. 52 (2015) 961–969. <https://doi.org/10.1080/00223131.2015.1038664>.
- [31] R.K. Salko, M.N. Avramova, CTF Theory Manual, the Pennsylvania State Univesity(2141).
- [32] S.J. Yoon, Extension of the Component Thermal- Hydraulics Analysis code CUPID toward Sub-channel Scale Analysis of PWR Reactor Core, Seoul National University, 2017.
- [33] K.J. Geelhood, W.G. Luscher, FRAPCON-4.0: Integral Assessment, Pacific Northwest National Laboratory. 2 (2015).
- [34] J. Choe, H.C. Shin, J.-E. Jung, J. Park, W. Kim, S. Choi, D. Lee, P. Zhang, H.S. Lee, Verification and validation of STREAM/RAST-K for PWR analysis, Nucl. Eng. Technol. 51 (2018) 356–368. <https://doi.org/10.1016/j.net.2018.10.004>.

- [35] S. Choi, D. Lee, Three-dimensional method of characteristics/diamond-difference transport analysis method in STREAM for whole-core neutron transport calculation, *Comput. Phys. Commun.* (2020) 107332. <https://doi.org/10.1016/j.cpc.2020.107332>.
- [36] S. Choi, D. Lee, Preliminary results for OPR1000/APR1400 whole-core analysis with neutron transport code stream, in: *Proceedings of M&C 2019 conference*, Aug. 25–29 (2019). [USB].
- [37] A. Yamamoto, T. Ikeno, Impact of pin-by-pin thermal-hydraulic feedback modeling on steady-state core characteristics, *Nuclear Technology*. 149 (2005) 175–188. <https://doi.org/doi:10.13182/NT05-A3588>.
- [38] Y.S. Jung, C.B. Shim, C.H. Lim, et al., Practical numerical reactor employing direct whole core neutron transport and subchannel thermal/hydraulic solvers, *Ann. Nucl. Energy*. 62 (2013) 357–374. <https://doi.org/10.1016/j.anucene.2013.06.031>.
- [39] A.M. Phillippe, A Validation Study of the AMP Nuclear Fuel Performance Code, thesis(master), University of Tennessee. [http://trace.tennessee.edu/utk\\_gradthes/1314](http://trace.tennessee.edu/utk_gradthes/1314).



## Acknowledgements

First of all, I would like to express my sincere gratitude to my thesis advisor Prof. Deokjung Lee of the Department of Nuclear Engineering at Ulsan National Institute of Science and Technology (UNIST). His continuous support and guidance since I started school at UNIST until completing the master's program helped in self-development, encouragement for thesis research, motivation, enthusiasm, insightful comments, and immense knowledge. I could not have imagined having a better advisor and mentor for my master's study.

Besides my advisor, I would like to thank the rest of the committee: Prof. Eisung Yoon and Prof. Douglas A. Fynan at UNIST for their insightful comments and questions, which encouraged me to look at my research from various perspectives.

I personally thank my senior Dr. Hyunsuk Lee, the main developer of MCS code in our group, for his lasting guidance, encouragement, patience, and his prompt support and help in understanding theoretical details in MCS as well as how MCS couple with other solvers.

I would also like to thank all my fellow seniors and lab mates: Dr. Peng Zhang, Dr. Matthieu Lemaire, Dr. Alexey Cherezov, Dr. Jiankay Yu, Dr. Xianan Du, Dr. Chidong Kong, Dr. Sooyoung Choi, Jiwon Choe, Wonkyeong Kim, Jinsu Park, Hanjoo Kim, Yunki Jo, Eun Jeong, Jaerim Jang, Kyeongwon Kim, Wonghee Lee, Dongmin Yun, Bamidele Ebiwonjumi, Nguyen Tung Dong Cao, Tuan Quoc Tran, Nhan Nguyen Trong Mai, Anisur Rahman, Siarhei Dzianisau, Setiawan Fathurahman, and all others for discussions and comments while working on my thesis and supporting my stay in Korea.

I take this opportunity to thank all faculty members and staff in the Department of Nuclear Engineering at UNIST for their help and support during my studies. Last but not least, I would like to thank my family for supporting me spiritually throughout my life. This accomplishment would not be possible without them.